NTNU – Trondheim
Norwegian University of
Science and Technology

Impurities in Ilmenite

Excess Iron

Sondre Norhaug

Materials Science and Engineering
Submission date: June 2015
Supervisor: Leiv Kolbeinsen, IMTE
Co-supervisor: Stephen Lobo, IMTE

Norwegian University of Science and Technology
Department of Materials Science and Engineering

Preface

This master's thesis has been carried out at the Department of Materials Science and Engineering at the Norwegian University of Science and Technology (NTNU) during spring 2015. This work is a continuation of the author's project work carried out autumn 2014, which was synthesis of iron rich ilmenite and how excess iron affects solid-state reduction. The introduction, theory and experimental chapters in this master's thesis are based on this project work [1].

Trondheim, 11th of June 2015

Sondre Norhaug

Acknowledgement

I would like to thank the following for their help and time:

Firstly, I am grateful to my supervisor, Leiv Kolbeinsen, for his weekly discussions, guidance, and theoretical help during this period. Secondly, Stephen Lobo deserves credit for all his help with both theoretical and experimental problems. His insight has been invaluable. Thirdly, I would like to thank Edith Thomassen (SINTEF) for her help with running the reduction furnace.

I would also like to thank Stian Seim for his help with experimental expertise and for helpful response to my questions. I am grateful for all the help from co-student Pyunghwa Kim with tackling challenges underway. My gratitude to Irene Bragstad (SINTEF) for her help with particle size analysis, Kristin Høydalsvik for help with XRD, Trygve Schanche for showing me how to prepare the EPMA samples, Morten Raanes for doing the EPMA and to Dmitry Slizovskiy for aiding with miscellaneous equipment. In addition, kind regards to the SiManTi(Al) group for providing valuable knowledge about how to present my work and other tips worth knowing when it comes to writing.

I would like to thank my classmates at study hall A-447 for making this last year fun. There has never been a dull moment. Finally, I would like to thank co-student Ole-Bjørn Ellingsen Moe for proofreading this thesis.

Abstract

During this master's thesis, batches of ilmenite with three different Fe/Ti-ratios were successfully synthesised. After synthesis, the batches underwent pre-oxidation, reduction with ThermoGravimetric Analysis (TGA), before subjected to an X-Ray Diffractometer (XRD) analysis and an Electron Probe MicroAnalysis (EPMA). These analyses produced degree of conversion graphs, XRD patterns, Backscattered Electron Images (BEI) and x-ray mapping of the elements. Two different gas compositions were used during reduction. These were 50% CO + 50% H_2 and 100% H_2. H_2 proved to enhance the reduction rate of ilmenite. Excess iron inhibits the rate of reduction and degree of conversion, however, only up to a certain Fe/Ti-ratio. Higher Fe/Ti-ratios will enhance the rate and conversion until they are equal to the rate and conversion of the reference ilmenite (Fe/Ti = 1.00). This occurs somewhere between Fe/Ti = 1.12 and 1.24.

Sammendrag

I denne masteroppgaven ble ilmenitt med tre forskjellige Fe/Ti-ratioer vellykket syntetisert. Etter syntesen ble de pre-oksydert før redusert med TermoGravimetrisk Analyse (TGA). Til videre analyse ble røntgendiffraksjon (XRD) og mikrosonde (EPMA) benyttet. Dette produserte konverteringsgrad grafer, XRD figurer, atomnummerkontrast analyse (BEI) og røntgenkart av de forskjellige elementene. To forskjellige gass-sammensetninger ble benyttet under reduksjonen. Disse var 50% H_2 + 50% CO og 100% H_2. H_2 viste seg å redusere ilmenitt mer effektivt. Ekstra jern hemmer reduksjonsraten og konverteringsgrad av ilmenitt, men kun opp til en viss Fe/Ti-ratio. Høyere Fe/Ti-ratioer enn dette øker reduksjonsraten og konverteringsgraden igjen til de blir like raten og graden til referanse ilmenitten (Fe/Ti = 1.00). Dette skjer et sted mellom Fe/Ti = 1.12 og Fe/Ti = 1.24.

Table of contents

List of figures

List of tables

Symbols/Glossary

Ar	Argon
B-N	Boron-nitride
C	Carbon
Fe	Iron
H	Hydrogen
O	Oxygen
Si	Silicon
Ti	Titanium

Chemical formulas

Anatase	TiO_2
Hematite	Fe_2O_3
Ferric pseudobrookite	Fe_2TiO_5
Ferrous pseudobrookite	$FeTi_2O_5$
Ilmenite	$FeTiO_3$
M_2O_3	α-oxide (Fe_2O_3 + $FeTiO_3$)
M_3O_4	Spinel (Fe_3O_4 + Fe_2TiO_4)
M_3O_5	Pseudobrookite (Fe_2TiO_5 + $FeTi_2O_5$)
Magnetite	Fe_3O_4
Magnéli phase, reduced rutile	$Ti_nO_{(2*n)-1}$, $(4 \leq n \leq 10)$
Pseudorutile	$Fe_2Ti_3O_9$
Rutile, titania	TiO_2
Ulvöspinel	Fe_2TiO_4
Wüstite	“FeO”

1 Introduction

1.1 Background

Titanium is the ninth most abundant element in Earth's crust [2]. It has a vast usage, ranging from the aero industry and automotive industry, to the production of pigment, paint, make-up, food, and others. Titanium is made from ilmenite ($FeTiO_3$) and rutile (TiO_2), with ilmenite as the major source (92% of the total production) [3]. Ilmenite is found in nature with many impurities depending on its localisation. These impurities affect the processing of ilmenite to rutile. The impurities of most importance are manganese, magnesium, and excess iron.

Natural ilmenite can occur as *rock ilmenite*. This has only been exposed to the weather and air in a minor degree, and it contains iron and impurities such as magnesium and manganese. Ilmenite can also be weathered, which is called *sand ilmenite*. It has been exposed to weather over time, and therefore some of its iron has been reduced. Ilmenite that has been completely weathered will be converted into rutile and is known as *beach ilmenite*.

Rock ilmenite is most commonly used in the industry due to its availability. However, new mines, such as Grande Côte in Senegal, are starting up using *sand ilmenite* [4]. Since titanium is made from rutile, the first step is to process the raw material into rutile by removing iron. A number of different processes are being used to accomplish this. Q.I.T. (Quebec Iron and Titanium) in Canada and RBM (Richards Bay Minerals) in South Africa charges the electric arc furnace with ilmenite and coal [5], while Australian companies mainly use the "Becher process" where metallic iron is removed from reduced ilmenite by leaching with water in air [6]. In Norway, the "Tyssedal process" is used. Here, the ore is first pre-reduced, similar to the first step of the "Becher process", with CO gas in a rotary kiln at 1100-1200°C, before cooled down, processed, and transported to the electric arc furnace (EAF) for smelting. From the furnace, the reduced iron smelt and the high titania (TiO_2) slag is tapped and further processed before shipped out [7]. One of the benefits from the Tyssedal process is that the iron content in ilmenite is recovered and sold as a valuable bi-product.

Studies have shown that the presence of H_2 in the reducing gas enhances the solid-state reduction of ilmenite [8] [9]. The combination of H_2 and CO gas is likely to give a more efficient reduction than only CO gas, which currently is being used in the pre-reduction process. However, further investigation is needed before the use of H_2 can be implemented in full-scale production.

Due to difficulty of synthesising pure ilmenite, there have been performed few studies isolating the influences of impurities during reduction. Previous experiments were reduction of natural ores, which contains variable amount of impurities, and the influences and mechanisms of these impurities are therefore not fully understood. A synthesised ilmenite can be a valuable pure reference material to which impurity elements can be added.

A recent study shows that synthesising stoichiometric ilmenite in a laboratory scale is possible. In Canaguier's master´s thesis [10], he was able to make synthetic ilmenite by using a composition of Fe, Fe_2O_3 and TiO_2 with a cold crucible induction furnace (CCIF). The study opens up an opportunity for adding impurities in a controlled manner and investigate the behaviour during solid-state reduction with CO and H_2 gas. This will make it possible to isolate the effect of individual impurities, which will lead to better understanding of the effect impurities have in natural ores.

The author has co-operated with co-student Pyunghwa Kim to gain a better understanding of the effect impurities in natural ilmenite have. Kim has been focusing on adding magnesium to ilmenite, while the author has been looking into the addition of iron. This is illustrated in **Figure 1** below, which is the quasi-ternary phase diagram for Fe-Ti-O-Mg. The red bottom triangle shows the area of focus for the addition of iron, while the blue triangle (perpendicular to the red triangle) is the area of focus for the magnesium rich ilmenite. As a mutual reference point for further comparison, the author and Kim have collaborated in making pure synthetic ilmenite.

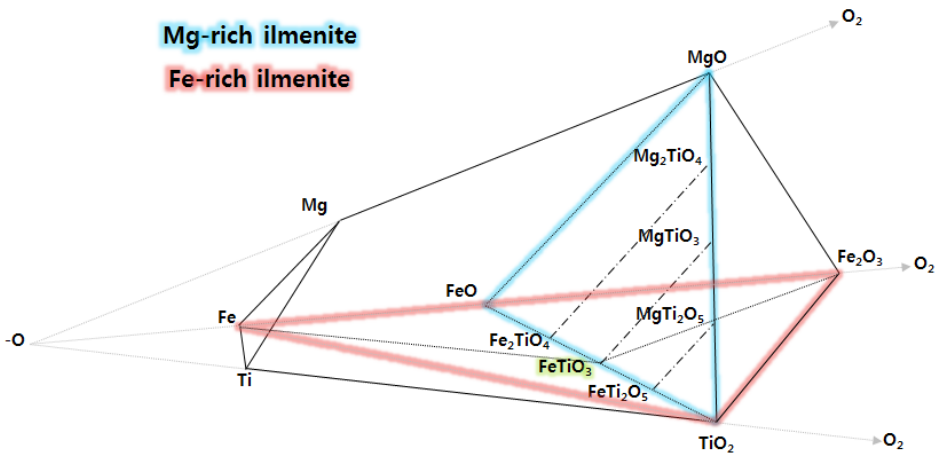

Figure 1: Quasi-ternary phase diagram for Fe-Ti-O-Mg

1.2 Scope of the thesis

The main objective of this work is to find a viable way to create iron rich ilmenite, and to find the reducing behaviour of synthesised ilmenite with the addition of different amounts of excess iron during solid-state reduction with CO and H_2 gas. This will be done by synthesis of ilmenite, crushing and pelletizing, before pre-oxidation and finally reduction. Many parameters can influence the reduction and have to be controlled. These are the synthesis environment, crushing time and particle size distribution, pellet size and the shape of the pellets, pre-oxidation conditions, and finally the reduction environment. To isolate the effect of excess iron, these parameters have to be kept constant.

1.3 Outline of the chapters

Chapter 2: Introduction of relevant thermodynamics, which will be the basis for the experiment. This will include an overview of the relevant phase diagrams and kinetics with the shrinking core model

Chapter 3: Setup of the experiments together with how the experiments were conducted. This chapter also includes information about the raw materials, together with the analysing-tools used.

Chapter 4: The results from the experiments are presented, and important results are noted.

Chapter 5: The experimental results from chapter 4 are discussed and compared with the theories obtained from the literature in chapter 2.

Chapter 6: The conclusions obtained from the experimental work are presented.

Chapter 7: The author's suggestion for future work.

Appendix: Theory and results that were not suited to be included in chapter 2 and 4, together with time schedules from the experimental work.

2 Theory

2.1 Degree of conversion

The degree of conversion is a measure of how much of the metallic oxide has been reduced. During this work, it is used to explain how much ferric Fe, Fe^{3+}, has been reduced to ferrous Fe, Fe^{2+}, and to metallic Fe. It will also show the rate of reduction. The following equation is used to calculate the degree of conversion:

$$Degree\ of\ conversion = \frac{\Delta mass\ loss_O(O\ from\ Fe-oxide)}{mass_{O\ tied\ to\ Fe\ at\ start\ of\ reduction}} \quad \textbf{(1)}$$

By this definition, when all the Fe - oxide is reduced to metallic Fe, the degree of conversion is one. It is possible to get a higher degree of conversion than one. This is believed to be a result of some of the Ti - oxide has become reduced. Degree of conversion is not to be confused with degree of metallization, which only tells how much metallic Fe is produced.

2.2 Synthesis

Synthesis of pure ilmenite have recently been done at NTNU by Canaguier [10]. It was done in a CCIF by melting metallic Fe, Fe_2O_3 and TiO_2 according to the following reaction:

$$Fe + Fe_2O_3 + 3TiO_2 = 3FeTiO_3 \quad \textbf{(2)}$$

2.3 Grinding and pelletizing

To produce ilmenite pellets suitable for pre-oxidation and reduction, the ilmenite needs to be grinded down and pelletized. During grinding the particle size and shape is changed, with the composition remaining the same. Ilmenite powder is inserted into a rolling drum together with a binder. The industry currently use water and bentonite as a binder. The particles are first wetted by the water, and the capillary forces bind them together. Bentonite is added to improve the strength of the pellets [11]. Water is sufficient as a binder for small-scale experiments.

2.4 Pre-oxidation

Untreated ilmenite pellets are called green pellets. Depending on the porosity of the green pellets, pre-oxidation will have varying effect on the reduction. If the green pellets have low porosity, the individual grains within are essentially single crystals. Pre-oxidation converts these crystals into polycrystalline arrays of pseudobrookite and rutile. This enhances the porosity and subsequently help the reducing gas to penetrate the pellet and reduce the core [12]. Green pellets with high porosity will not gain any noticeable reduction-effect from pre-oxidation. However, the main reason for pre-oxidation in the industry is its use for hardening the pellet and making it durable. It will sinter the pellets, making them tougher to be broken due to pressure and shock.

Below 800^{O}C the following reactions will take place [13]:

$$4FeTiO_3 + O_2 = 2Fe_2O_3 + 4TiO_2 \quad \textbf{(3)}$$

$$12FeTiO_3 + 3O_2 = 4Fe_2Ti_3O_9 + 2Fe_2O_3 \quad \textbf{(4)}$$

Above 800^{O}C, the following reactions will take place [14]:

$$4FeTiO_3 + O_2 = 2Fe_2TiO_5 + 2TiO_2 \quad \textbf{(5)}$$

$$Fe_2Ti_3O_9 = Fe_2TiO_5 + 2TiO_2 \quad \textbf{(6)}$$

Pseudorutile, $Fe_2Ti_3O_9$, is an intermediate step, which will not be present in the fully oxidized sample. It has been shown that ferric pseudobrookite, Fe_2TiO_5, is the most desirable oxidation product [12]. In addition, Pseudobrookite is the most stable product at 1000^{O}C. However, studies have shown that lower concentration of hematite, Fe_2O_3, also to be present after pre-oxidation [1, 15].

2.5 Reduction

With the starting point being Fe_2TiO_5, metallic Fe is formed at 1000°C during reduction in two steps according to reactions **(7)** and **(8)**. R is the reducing gases, CO and H_2. According to Jones [14], the reduction reaction starts from ferric Fe to ferrous Fe, before ferrous Fe is reduced to metallic Fe. Reaction **(8)** implies that the product of ilmenite reduction should be Fe and TiO_2. However, ilmenite with impurities is likely to form other products and thus, hindering the production yield.

$$Fe_2TiO_5 + TiO_2 + R = 2FeTiO_3 + RO \quad \textbf{(7)}$$

$$FeTiO_3 + R = Fe + TiO_2 + RO \quad \textbf{(8)}$$

If any Fe_2O_3 is formed during oxidation it can be reduced to "FeO" according to reaction **(9)** below [9]. "FeO" is more accurately written $Fe_{1-x}O$, due to vacancies within the Fe lattice. However, for simplicity "FeO" is used in the reactions below.

$$Fe_2O_3 + R = 2"FeO" + RO \quad \textbf{(9)}$$

Before finally being reduced to metallic Fe:

$$"\mathrm{FeO}" + R = Fe + RO \quad \textbf{(10)}$$

During reduction with CO gas the Boudouard reaction will occur:

$$2CO = CO_2 + C \quad \textbf{(11)}$$

However, as long as there is ilmenite to be reduced, the reaction will shift towards left and carbon will not be produced. After the ilmenite has been reduced, further reduction with CO gas may cause some carbon to be produced. According to Kucukkaragoz and Eric [16], Fe_3C can be formed during reduction with carbon.

Study shows the presence of H_2 in the reducing gas enhances the reduction rate of ilmenite [8].

Zhao and Shadman [17, 18] have done studies on ilmenite that has not been pre-oxidized, where the Fe is in its ferrous state. This shows that during reduction, metallic Fe produced is distributed in the pores at the TiO_2 layer. This metallic Fe has a higher activity than the metallic Fe on the boundaries of the grain particles. Small Fe islands are less stable than larger agglomerated islands, and they will therefore diffuse towards the larger agglomerates of metallic Fe. In addition, Zhao and Shadman suggest reduction follows three stages, the initial stage, acceleration stage and deceleration stage.

The rate of the initial stage depends on the nucleation and growth of Fe-phases. The production rate of Fe from $FeTiO_3$, which occurs according to reaction **(8)**, is faster than the transport rate of Fe out of the TiO_2 layer. Therefore, the Fe will partially occupy pores within the TiO_2 layer and hinder the reduction by not allowing the reducing gas to enter. However, this effect is more significant for CO than for H_2 reduction. Excess Fe enhances the nucleation and growth of Fe-phases, subsequently increasing the reduction rate of the initial stage.

The acceleration stage occurs when more Fe nuclei are formed, which increases the growth rate of Fe phases. Due to this, the transport of Fe is enhanced. This leads to the pores within the TiO_2 layer to be emptied, which opens up for the reducing gas to enter. As a result, rate of reduction increases.

The deceleration stage is the final stage, where due to depletion of $FeTiO_3$, the rate of reduction is decreased.

2.6 Void fraction

A two-component particle mixture have different void fractions depending on the difference between the size of the particles and the volume fraction of these. A graph illustrating this correlation is shown below in **Figure 2**:

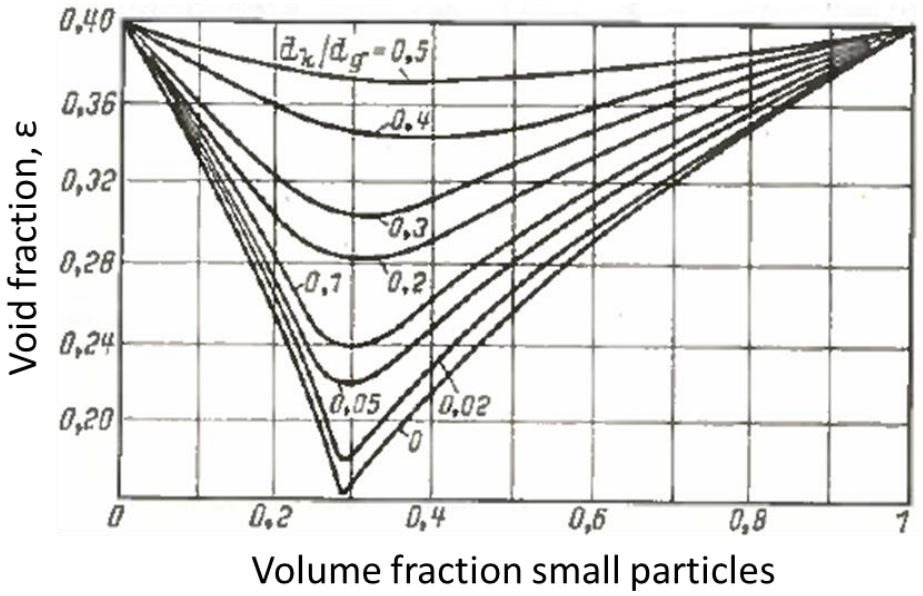

Figure 2: Void fraction over volume fraction for small particles [19]

Here d_k and d_g is sphere diameter for small and large particles respectively. As shown in the graph above, a volume fraction of $2/3$ coarse particles and $1/3$ fine particles is the optimal packing to get the densest mixture. It can also be seen that the densest mixture is accomplished if the ratio d_k/d_g is as low as possible.

2.7 Sintering of TiO_2

Sintering is the densification of a component. Pores within a material is removed, together with shrinkage of the whole material. Adjacent particles within the material are grown together and forms a strong bond. Two things must be present to accomplish sintering. A mechanism for material transport, diffusion or viscous flow, and a source of energy to activate this transport mechanism, which is usually heat. During solid-state sintering diffusion is the driving mechanism [20].

Sintering occurs in three stages: the initial stage, intermediate stage and final stage. During the initial stage, particles are rearranged so that number of contact points are increased. At the contact points between each particle initial neck formation occurs. The next step is the intermediate stage. Here the necks and the grain grows. The total volume of the material shrink due to lower porosity. At the final stage, the grain grows larger and the pores are being reduced to nearly complete elimination. These three stages are shown in **Figure 3** below.

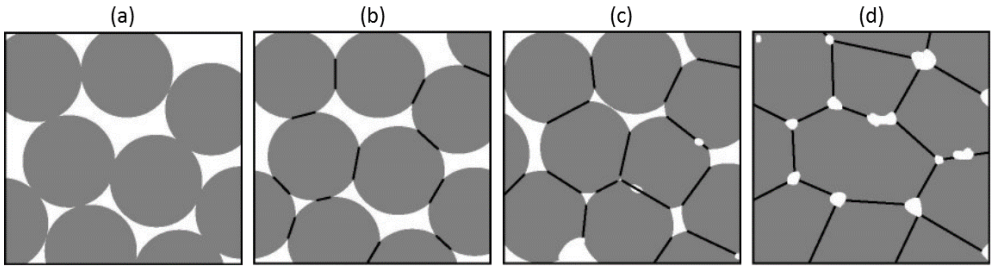

Figure 3: Stages of sintering
(a) *untreated powder, (b) initial stage, (c) intermediate stage and (d) final stage [21].*

Study has shown that diffusion at low temperature leads to the disappearance of small pores in TiO_2 [22]. At 600^{O}C, the removal of pores increases the density noticeably, while at 900^{O}C the density reaches its theoretical value. The study also shows that the grain growth has increased with temperature. At 600^{O}C, the grain growth becomes sufficiently large to influence sintering, while at 1000^{O}C the grain growth increases rapidly. Sintering under pressure has also shown to enhance the achieved density.

2.8 Phase diagram

The Fe-Fe_2O_3-TiO_2 system has been studied in some extent by Borowiec and Rosenqvist [23] and Itoh [24]. Based on their work the author has re-illustrated the Fe-Ti-O phase diagram below, outlining the areas of interest.

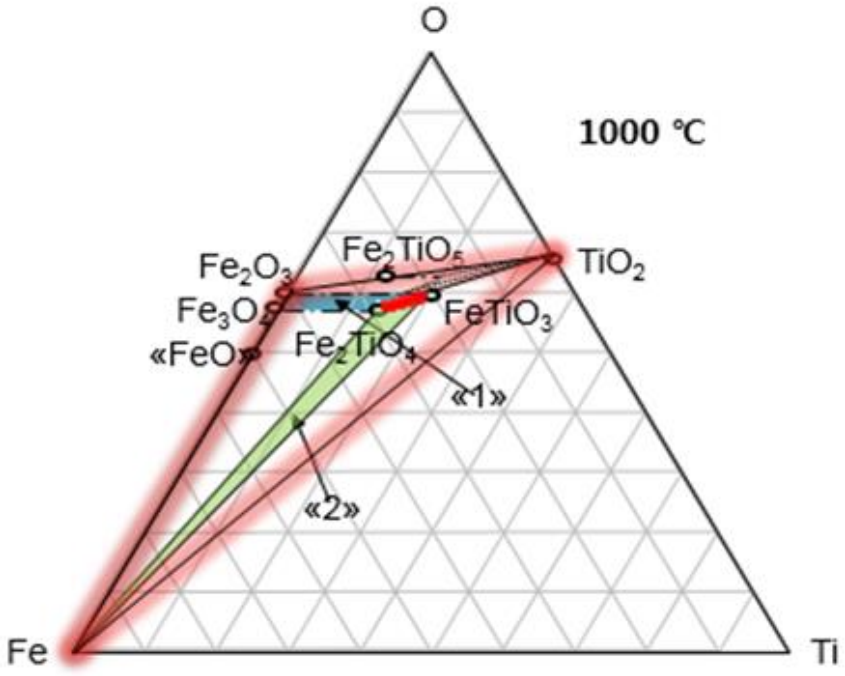

Figure 4: The Fe-Ti-O system at 1000^{O}C

Figure 4 shows the Fe – Ti – O phase diagram at 1000^{O}C, with the phases Fe – Fe_2O_3 – TiO_2 in more detail. The areas of interest are the two three-phased areas "1" and "2", and especially the boundary line between these two areas. "1" is the α – oxide + spinel area, while "2" contains Fe + spinel + α – oxide. α – oxide is a M_2O_3 phase, which can be both $FeTiO_3$ and Fe_2O_3. Spinel is a M_3O_4 phase, Fe_3O_4 and Fe_2TiO_4. The line in-between these areas will be a solid solution of Fe_2TiO_4 and $FeTiO_3$. In **Figure 5**, the area in question is enhanced. The red line is the boundary line between the three-phase and the two-phase area of interest.

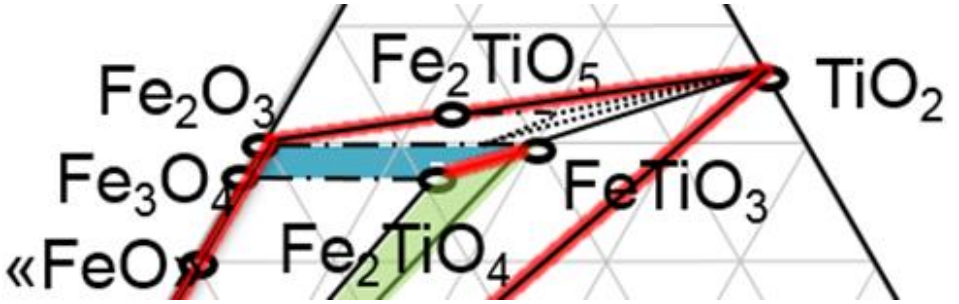

Figure 5: The enhanced Fe-Ti-O system at 1000^{O}C

During oxidation, oxygen is added to the sample, which means the composition will shift upwards in the phase diagram above. First the composition will enter into an α – oxide + Fe_2TiO_5 + TiO_2 phase before complete oxidation according to reaction **(5)** and **(6)** and form Fe_2TiO_5 + TiO_2. The reduction is likely to follow reaction **(7**) and **(8)**. After full reduction, oxygen tied to the Fe is removed from the sample and the composition will be Fe + TiO_2, with the possibility of some reduced TiO_2.

2.9 The crucible

A special crucible is required to withstand chemical reaction between the high-titania slag and the crucible, due to the titania slags highly corrosive nature. It is important to maintain a freeze lining to prevent an interaction with the crucible, since this could damage it greatly [10, 25]. As a result, standard refractories will be dissolved by the slag, which means other refractories are needed. Previous work at NTNU has been successfully done in a continuously water-cooled copper crucible, with a thin boron-nitride coated layer. This was done by Seim [26] and Canaguier [10]. Due to these previous successes with the copper crucible, the same setup was chosen in this master's thesis.

2.10 Kinetics

The reduction of a solid with gas occurs according to the follow reaction [27]:

$$aA\,(s)\ +\ bB(g)\ =\ sS(s)\ +\ rR(g) \qquad \textbf{(12)}$$

The solid particles can either remain unchanged in size or shrink during reaction according to **Figure 6**.

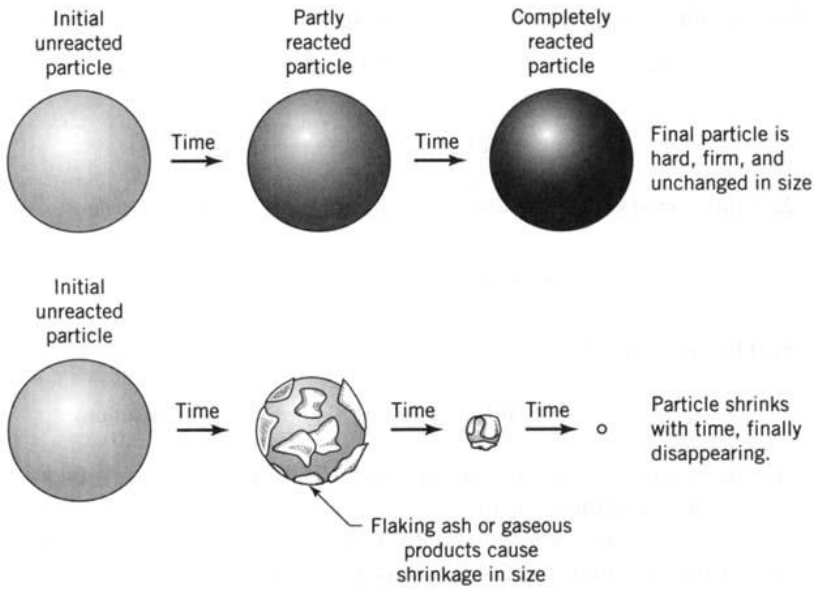

Figure 6: Reaction behaviour of a solid particle

If the particles contains a large amount of impurities that remain as a non-flaking ash or form a firm product layer, the particles will stay unchanged in size. An example of this is the creation of iron from magnetite in a fluidized-bed reactor

$$Fe_3O_4(s)\ +\ 4H_2(g)\ \rightarrow 3Fe(s)\ +\ 4H_2O(g) \qquad \textbf{(13)}$$

If the particles that are reduced forms a gas or flaking product ash, they will shrink in size during reaction. This happens during burning of carbon

$$C(s)\ \rightarrow\ C(g) \qquad \textbf{(14)}$$

There are a number of different models to describe what happens with the solid particle during reaction, with varying degree of complexity. Although there might be models that follows what happens with the particle in reality, they might be too complicated to use. A good model is close to reality, simple, and easy to use. Following are two simple idealized models, the progressive-conversion model and the shrinking core model.

2.10.1 Progressive-Conversion Model (PCM)

In this model the reacting gas enters the solid particle and reacts throughout the particle at all times [28]. The reduction happens at different rates, depending on the location inside the particle. This means the solid particle is reduced and converted continuously throughout the particle as shown in **Figure 7** below.

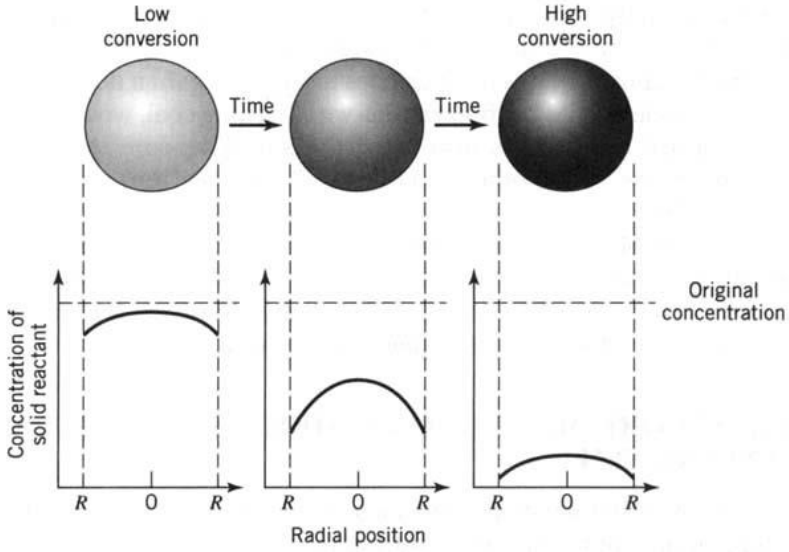

Figure 7: Progressive-conversion model [28]

Although PCM is a good model, it has not been the model of choice for describing the kinetics inside a pellet during reduction of ilmenite. In literature, to describe this the shrinking core model has been widely accepted as the best way.

2.10.2 Shrinking Core Model (SCM)

This model was first introduced by Yagi and Kunii in 1961 [29]. It is often a good model to use because it describes the behaviour of real particles with reasonable accuracy and is simple to use. The SCM consists of five steps, as visualized in **Figure 8** below. They are:

1. Diffusion of gas from bulk to outer surface, through a stagnant gas film.
2. Diffusion through the porous product layer towards the interface of the unreacted core.
3. Chemical reaction at the interface between the ash layer and the unreacted core.
4. Diffusion back through the porous product layer to the outer surface.
5. Diffusion of gas from the outer surface to the bulk, through the stagnant gas film.

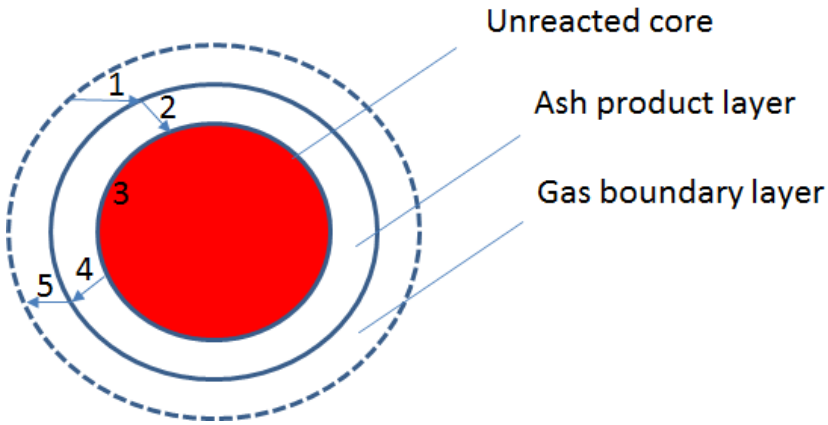

Figure 8: Shrinking core model for spherical particles of unchanging size

Each of these steps has a varying degree of resistance, depending on many factors. The step with the greatest resistance is the rate-limiting step. Equations below and the complete derivations of these are done by Levenspiel [27, 28]. For the reaction **(12)**, the following three resistances are in series.

Diffusion of A through the gas film

$$-\frac{1}{S_{exterior}}\frac{dN_A}{dt} = k_g\left(C_{A,g} - C_{A,s}\right), where\ k_g has\ dimension\ \frac{m}{s} \quad \textbf{(15)}$$

Diffusion of A through the ash layer

$$-\frac{1}{S_{at\ any\ r}}\frac{dN_A}{dt} = D_e\frac{dC_A}{dr}, where\ D_e has\ dimension\ \frac{m^2}{s} \quad \textbf{(16)}$$

Chemical reaction at the interface between the ash layer and the unreacted core

$$-\frac{1}{S_{at\ core}}\frac{dN_A}{dt} = k_s C_{A,c}, where\ k_s has\ dimension\ \frac{m}{s} \quad \textbf{(17)}$$

Here we have N_x = amount of x in mole, k_x = mass transfer coefficient for x, S_x = surface x, and D_e = diffusion coefficient of A through the ash layer. We use the kinetic parameter τ, the time for complete conversion of the particle, to represent the conversion rate during a gas/solid reaction.

Rate-limiting steps

Based on equation **(15)**, **(16)** and **(17)** the following conversion expressions $\frac{t}{\tau}$ can be derived. Detailed calculations are shown in Appendix B. X_B = conversion level for a particle, r_c = radius of unreacted core, R = radius of particle, $C_{A,g}$ = concentration of reactant in gas and ρ_B = the molar density of B.

Table 1: Conversion rate for the different rate-limiting steps

Diffusion of A through the gas film	$\frac{t}{\tau} = X_B,$ $where\ \tau = \frac{R\rho_B}{3bk_gC_{A,g}}\ and\ X_B = 1-\left(\frac{r_c}{R}\right)^3$
Diffusion of A through the ash layer	$\frac{t}{\tau} = 1-3\left(\frac{r_c}{R}\right)^2+2\left(\frac{r_c}{R}\right)^3$ $= 1-3(1-X_B)^{\frac{2}{3}}+2(1-X_B)$ $where\ \tau = \frac{\rho_B R^2}{6bD_eC_{A,g}}$
Chemical reaction at the interface between the ash layer and the unreacted core.	$\frac{t}{\tau} = 1-\frac{r_c}{R} = 1-(1-X_B)^{1/3},$ $where\ \tau = \frac{\rho_B R}{bk_sC_{A,g}}$

Guide to determine the rate-limiting step

There are different ways to determine which step is rate-limiting, and following are different observations given by Levenspiel [27, 28] to help determine this.

Comparing by plotting

By plotting your data as $\frac{t}{\tau}$ and comparing this line with the curves formed from the equations in **Table 1**, it is possible to evaluate which of the equations fits the data best. Unfortunately, the ash diffusion and chemical reaction equations are too similar in shape. Other methods needs to be used to distinguish between these two.

Film diffusion vs ash layer diffusion

When a hard solid ash layer forms during reaction, the ash layer diffusion is usually the rate-liming step. This is because the resistance between gas/solid in the ash layer is much higher than the resistance gas/gas in the gas film.

Temperature

The chemical step is usually more dependent on temperature than the two others are. Because of this, it is possible to determine which step is rate-limiting by varying the temperature. If the reaction varies significantly either way during the change in temperature, one can assume the chemical step is the rate-limiting. If the structure of the solid changes due to the change in temperature, i.e. sintering, diffusion through the ash layer can become the rate-limiting step.

Particle size and conversion

From the equations in **Table 1**, it can be derived that the time to reach any conversion level of X_B for particles of different and unchanging size, are as follows:

$$t \propto R^{1.5\ to\ 2.0}\ for\ film\ diffusion\ limiting$$

$$t \propto R^2\ for\ ash\ layer\ diffusion\ limiting$$

$$t \propto R\ for\ chemical\ reaction\ limiting$$

When considering ash layer versus chemical reaction, it is more likely that the ash layer is the rate-limiting step with increasing particle size R based on the relation between time and radius above. Taking data of solids with different sizes is an easy and good method for figuring out which of these mechanics is the controlling one.

Notes about the Shrinking Core Model

The simple shrinking core model for unchanging size describes the reducing behaviour with one reducing gas and one intermediate phase. However, for synthetic ilmenite reduction with H_2 and CO there are two reducing gases and two intermediate phases. This will increase the complexity of the model. During this master's thesis, the complex model will not be discussed.

3 Experimental

Each synthesis created 300g of ilmenite, but 600g were needed from each Fe/Ti-ratio to get enough materials for the succeeding steps. Therefore, two identical syntheses of each Fe/Ti-ratio had to be successful in order to achieve this. Notation for the batches will be "**Batch #A.B.C**", where "**A**" shows the Fe/Ti-ratio, while "**B**" shows which synthesis attempt at "**A**". An "**X**" is used at position "**B**" where two identical syntheses have been made and mixed. The "**C**" is what reducing gas mixture was used.

For example, **batch #3** has a Fe/Ti-ratio equal 1.12. If attempt number 3, **#3.3**, and 4, **#3.4**, were successful and identical, they were mixed. Instead of writing batch **#3.3-3.4**, they are denoted as **#3.X** for simplicity. **Batch #3.X** was split in two and reduced with two different gas compositions. **Batch #3.X.1** was reduced with 50% CO + 50% H_2 and **#3.X.2** with 100% H_2. All other batches were done with 50% CO + 50% H_2. Therefore, the ".1" at the end of **batch #4.X** and **#5.X** is removed for simplicity.

3.1 Raw materials

Different raw materials were attempted for synthesis of Fe rich ilmenite, with varying degree of success. These are presented below.

3.1.1 Magnetite

Magnetite powder is dark in colour, and is a mix of ferric and ferrous Fe. It oxidize at low temperatures, and can oxidize at room temperature if kept for a longer period of time. [30]. Oxidation of magnetite is a highly exothermic reaction. Therefore, drying in an oxygen-rich atmosphere will lead to the magnetite being oxidized to hematite. Magnetite will change to γ-hematite, also known as maghemite, below 500^{O}C. Above this temperature α-hematite is produced, with the transformation completed between 900-1100^{O}C. Hematite will be dissociated back to magnetite above 1200^{O}C. Research shows that to prevent magnetite from oxidizing it has to be kept at -50^{O}C [30]. This will create a problem when it comes to removing water-residues from the magnetite powder by drying. An inert atmosphere have to be obtained to prevent the magnetite to oxidize. Due to this, the experiments with magnetite failed. These experiments will not be presented in this master's thesis.

3.1.2 Hematite

Hematite powder has a distinct red colour. All the Fe is in its ferric state; therefore, no further oxidation can occur. The powder used had a size of >5µm, with a purity of >99.00%.

3.1.3 Rutile and anatase

Rutile is white in colour. During these experiments granulates with purity >99.90% and size range of 1-4 mm was used. All of the successful batches, except **batch #5.3**, were conducted with the use of granulates. **Batch #5.3** was done with an anatase powder with purity >99.00% and size >5µm. Anatase has the same stoichiometric composition as rutile, but with slightly different lattice parameters. This powder was briquetted and sintered before used in the synthesis, and will be explained in greater length further down in this chapter. The anatase into rutile transformation occur slowly below 610°C and quite rapidly above 730°C [31]. It is also enhanced with the presence of Fe^{3+} under argon atmosphere [32], and complete transformation should be achieved under the current experimental conditions. In addition, anatase is not believed to have any negative effect on pre-oxidation and reduction. Therefore, anatase powder was used as a substitute for rutile.

3.1.4 Iron metal

Iron metal has a metallic colour and a density of 7.874 g/cm^3. The pieces dimensions were approximately 3.2-6.4 mm and had a purity of >99.99%.

3.2 Composition

This study has been conducted with three different Fe/Ti-ratios, shown in **Table 2. Batch #4.X** was made with the intention of creating pure ilmenite, $FeTiO_3$, as a reference material for further investigation. **Batch #1.X** was synthesised during the authors project work [1] and is identical to **batch #4.X.** It is used in this master's thesis to compare the Electron Probe MicroAnalysis (EPMA) results for reference ilmenite reduced over two different periods of time. Both **batch #1.X** and **#4.X** were reduced in a 50% H_2 + 50% CO atmosphere. Further, the intention was to change the Fe addition to give different Fe/Ti-ratios. Previous work by the author, where Fe rich ilmenite was made by addition of only metallic Fe, proved to introduce a problem with the agglomeration of Fe at the bottom of the synthetic ilmenite, creating a Fe "button". This created problems during crushing and the Fe "button" had to be discarded. Therefore, during this master's thesis, Fe rich ilmenite was created by adding equal moles of Fe_2O_3 and metallic Fe.

Batch #3.X had a Fe/Ti-ratio equal 1.12. This was chosen due to this ratio being approximately the same Fe/Ti-ratio found in the Tellnes ilmenite used at TiZir in Tyssedal. For **batch #3.X.1,** reduction was done in a 50% H_2 + 50% CO atmosphere, while batch **#3.X.2** had a 100% H_2 atmosphere.

Batch #5.X had a Fe/Ti-ratio equal 1.24 and reduction was done in a 50% H_2 + 50% CO atmosphere. **Batch #3.X.1**, **#4.X** and **#5.X** were done to observe how excess Fe affected the solid-state reduction of ilmenite, while **batch #3.X.2** was conducted to show the impact H_2 as the reducing gas has on the reduction.

Table 2: Batch compositions for synthesis

Batch #	Fe		Fe_2O_3		TiO_2		Total	Fe/Ti
	gram	moles	gram	moles	gram	moles	gram	ratio
#3.3	39.01	0.70	111.54	0.70	149.45	1.87	300.00	1.12
#3.4	39.03	0.70	111.51	0.70	149.46	1.87	300.00	1.12
#4.1	36.80	0.66	105.25	0.66	157.95	1.98	300.00	1.00
#4.3	36.80	0.66	105.24	0.66	157.94	1.98	299.98	1.00
#5.3	41.02	0.73	117.18	0.73	141.85	1.78	300.05	1.24
#5.4	41.00	0.73	117.16	0.73	141.85	1.78	300.01	1.24

3.3 Briquetting

Due to lack of >5µm granulated rutile, an alternative synthesis with TiO_2 – powder was attempted. This proved difficult, due to the volume becoming greater than what the crucible could hold. The batch size had to be reduced to approximately 150-170 g, which would lead to too little metallic Fe to be placed in the crucible. This amount of metallic Fe was not sufficient to get a good smelt during induction. In addition, if the crucible is filled completely up with raw materials, the Fe pieces are too high up in the crucible, out of reach for the induction coil. This lead to an insufficient low temperature, which in turn results in an incomplete smelt. As a solution, briquetting of the oxides was attempted.

Briquetting is done with C-press, which is a hydraulic press, shown in **Figure 9**. Two different pistons with different diameters were used, 15 mm and 50 mm, to make small and large briquettes respectively. The 50 mm piston is shown in **Figure 10.** The oxides were inserted into the pistons and a pressure was applied, 2.5 metric tons for the 15 mm and 5.5 metric tons for the 50 mm. For both pistons the pressure was kept for 1.5 minutes. The briquettes produced weighted 3-4g from the small piston and 40g for the large piston. During pressing, different pressure-gradients were introduced to the briquettes, which resulted in voids and deformation within. Stearic acid was used as a lubricant for the pistons in order to prevent any damage on the equipment during pressing.

Figure 9: Hydraulic press

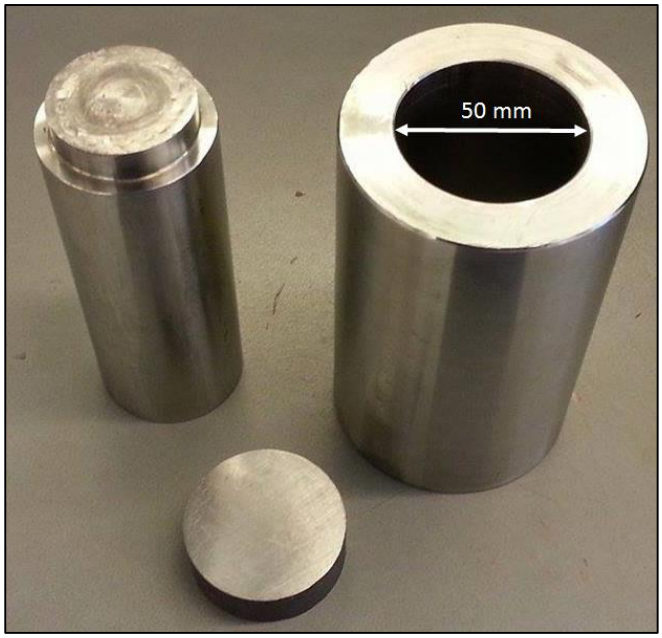

Figure 10: 50 mm briquetting piston

The author attempted different methods to make use of the TiO_2 – powder. The factors that were changed was the size of the briquettes, amount of powder versus briquettes and which of the oxides were briquetted.

Attempt #1.1 was done with small sized TiO_2 briquettes. These were made without sintering or any other heat-treatment and positioned in the crucible layer by layer together with Fe_2O_3.

Attempt #1.2 was done with small sized briquettes of the oxide mixture, Fe_2O_3 + TiO_2. These briquettes together with a small amount of powder were heat treated at 100°C in order to remove any water-residue. The extra powder was used to fill up the gaps created when the briquettes were positioned in the crucible.

Attempt #1.3 was done as **attempt #1.2**, but with large sized briquettes instead of small.

Attempt #2.1 was done with large briquettes of TiO_2. These were sintered and broken up to smaller pieces, mixed with Fe_2O_3 powder and positioned in the crucible.

3.4 Sintering

The furnace used for sintering was a muffle furnace, Nabertherm N17/HR, shown in **Figure 11**. Pressed briquettes of TiO_2 were put in a steel pan, inserted into the furnace, before heated to 900°C and held at that temperature for 15 hours. After the heat-treatment, the briquettes were air-cooled down to room temperature. The stearic acid used during briquetting might leave residual traces on the TiO_2. However, the boiling temperature for stearic acid is 361^{O}C [33], therefore it is believed to be fully removed during sintering.

Figure 11: Nabertherm N17/HR

3.5 Synthesis

The synthesising of the samples was done in a CCIF. It consists of a power supply from Farfield Electronics PTY Ltd and a continuously water-cooled copper crucible from Australian Nuclear Science and Technology Organisation (ANSTO), shown in **Figure 12**. This equipment has previously been used for synthesis of ilmenite by Canaguier [10] and for ilmenite slag by Seim [26].

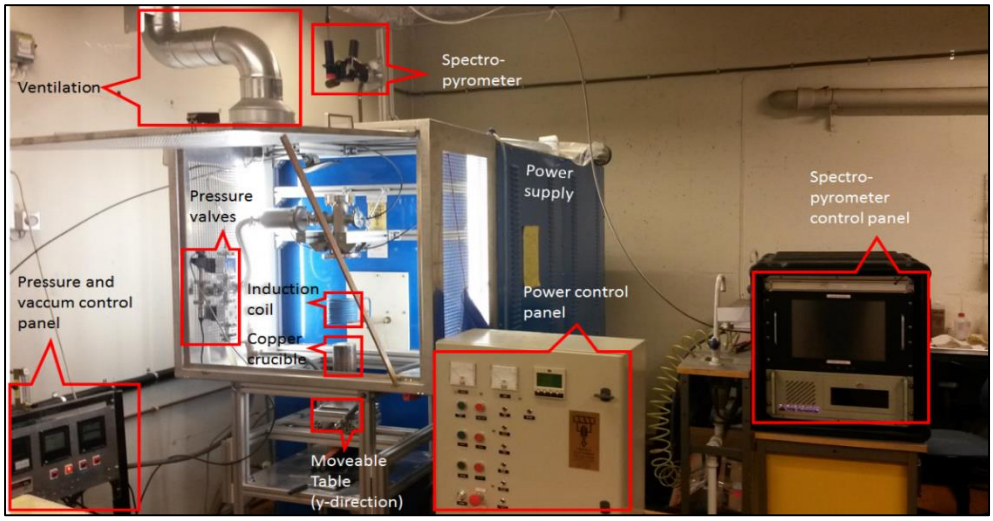

Figure 12: CCIF used for synthesis

The crucible was coated with boron-nitride (B-N) to prevent the copper "fingers", as shown in **Figure 13**, to be in contact with each other and create small electric arcs during synthesis. The use of coating also hinders the sample to stick to the crucible, which makes sample extraction easier after synthesis. The B-N coating was added as a paint and dried overnight, which would leave an all-covering thin dry white layer on the inside of the crucible.

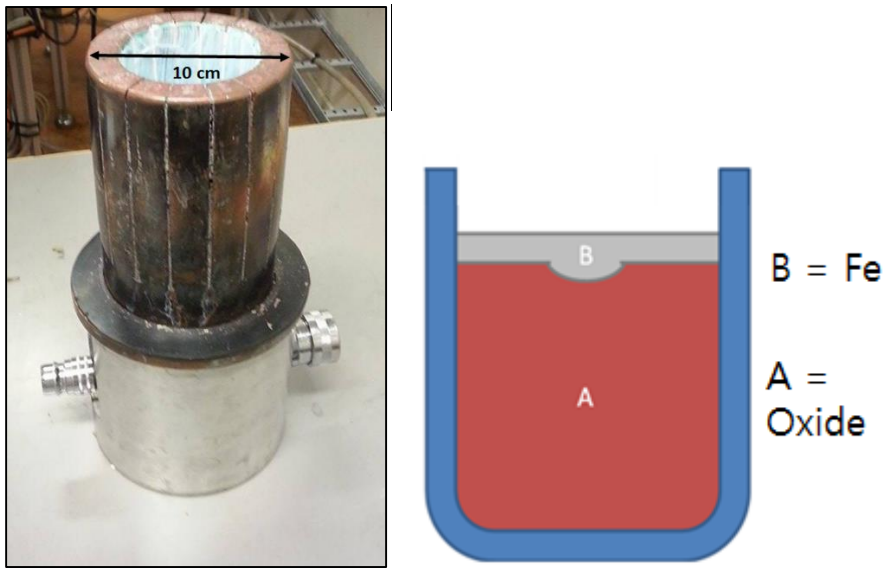

Figure 13: The crucible
Coated copper crucible for CCIF (left). Positioning of iron and oxides in the crucible (right)

After the coating was applied, the crucible was filled with the raw materials. This was done, as described by Canaguier [10], by mixing the oxide together for ten minutes in a Turbula mixer before adding this to the bottom of the crucible. Metallic Fe was positioned on top of the oxide, as shown in **Figure 13**. The optimal packing structure in the crucible to avoid significant voids depends on the size of the materials being mixed, and their respective volume fraction [19]. As seen in **Figure 2**, the greater size difference between the oxides, the better. This had to be taken into consideration when filling the crucible.

The current runs through the induction coil, and causes fluctuation in the magnetic field. This will heat the metallic Fe. When the metallic Fe melts, it will sink down towards the bottom while melting the oxide layer. This way an oxide crust on top was avoided and all the oxide was melted. An argon atmosphere was introduced to the sealed system to avoid any oxidation during the synthesis. The surface temperature was measured and logged by using a spectro-pyrometer. Previous study [10] show that a temperature of 1600-1700 ^{O}C was sufficient, which corresponded to a current intensity of approximately 70%. This temperature was kept for 5 minutes prior to decreasing the current to zero. The crucible and sample was then cooled by water before dismantling the setup and removal of the sample.

3.6 Pelletizing

The samples were crushed and pelletized prior to pre-oxidation and reduction. It was first crushed in a mortar before put into a ring and puck crusher. Crushing time was 24 seconds, turning it into a fine powder. This powder was used in a pelletizing drum together with a binder. To avoid additional impurities water was used as a binder. Pelletizing was done with help from Edith Thomassen (SINTEF) and the final product was pellets with a diameter of 9-10 mm. The pellets were then dried in a heating cabinet overnight to remove the water. Mass loss due to crushing and pelletizing was about 10-30%.

3.7 Pre-oxidation

Pre-oxidation was done in the same furnace as sintering. This is a muffle furnace, Nabertherm N17/HR, shown in **Figure 11**. The pellets were put in a steel pan container and inserted into the furnace. The temperature was then constantly increased for one hour until it reached 1000^{O}C. This was done to avoid possible cracks to occur due to thermal shock. The temperature was kept at 1000^{O}C for one hour before air-cooling the sample down to room temperature.

3.8 Reduction

To reduce the pellets a vertical retort ThermoGravimetric Analyser (TGA) DiSvaDRI furnace was used. A sketch of the retort, copied from Zhao [34], together with a picture of the TGA is shown in **Figure 14**.

The setup consists of a retort that is suspended into an Entech resistance furnace model VTF 801/12. Three thin wires connects the retort with a balance, a Mettler Toledo model PR2003DR. The retort is also connected to two tubes that transports the gas in and out. To control the gas flow Bronkhorst model F201c mass controllers are used. To ensure an accurate temperature measurement, a sheathed thermocouple is submerged halfway inside the sample. A computer is used to log and control the experimental conditions. The gas enters the double-sided wall at the top and travels to the bottom of the retort while being heated. A small porous table with the sample on top is situated at the bottom of the retort. The heated gas hits the pellets, which will be reduced if a reducing gas is used. The gas then travels up in the middle of the retort, before leaving through a connected gas tube at the lid. The mass loss is automatically measured and logged by the connected computer.

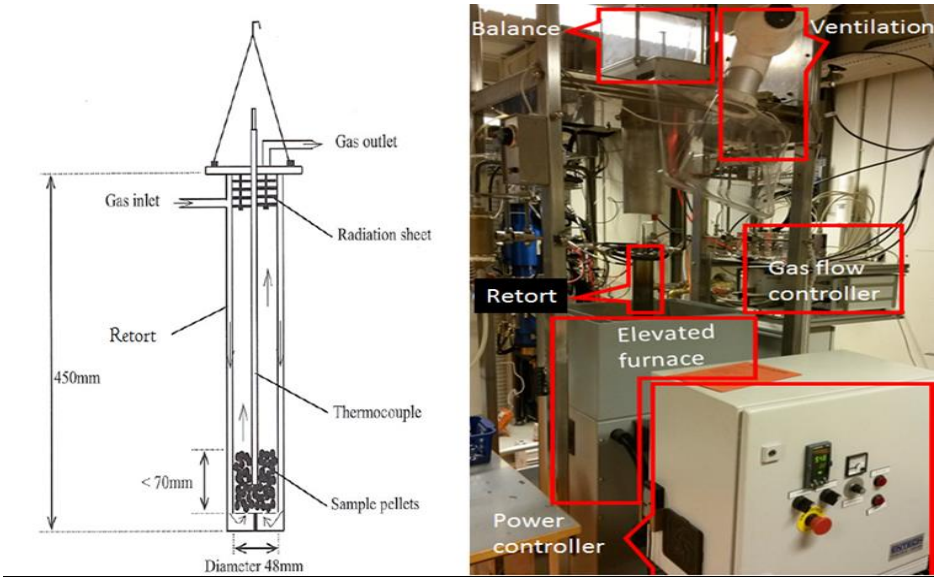

Figure 14: The TGA Retort [34] (left). DiSvaDRI Furnace (right)

Experimental conditions for the reductions are shown in **Table 11**, **Table 12** and **Table 13** in appendix A.1. Two different gas combinations were used. For **batch #3.X.1**, **#4.X** and **#5.X** a mixture of 2.5 l/min CO + 2.5 l/min H_2 and for **batch #3.X.2** 5 l/min of H_2. **Batch #1.X** was reduced during previous work with 2.5 l/min CO + 2.5 l/min H_2. To get an inert atmosphere before and after reduction, argon gas was used. The set-point of the furnace was 958^{O}C, due to previous work has shown 958^{O}C as a set-point will give a sample temperature of 1000^{O}C [10]. The sample was weighed before mounting and after dismantling of the retort. In addition, the equipment was mounted in advance to let the wires and retort stabilize. **Batch #1.X** was reduced for 40 minutes, while **#4.X** and **#3.X.2** were reduced for 160 minutes. It was clear after reduction of **batch #4.X** that a reduction time of 120 minutes was sufficient to get a full reduction when 50% CO + 50% H_2 was used. Therefore, **batch #3.X.1** and **#5.X** were only reduced for 120 minutes. Reduction was done with help from Edith Thomassen (SINTEF) and Stephen Lobo (NTNU).

3.9 Analysis

3.9.1 X-ray diffraction

A small sample of approximately five grams was extracted from each of the above steps, crushed into a powder and analysed in an X-Ray Diffractometer (XRD). The equipment used was the Da Vinci XRD. The scans were performed from 10 to 75 2θ for 30 minutes with a varying slit and a step size of 0.0181 degrees per second, before the analysis was evaluated and the phases determined using the Diffracplus EVA software. This is done by comparing the diffraction angles θ measured in the sample with those of known compounds in the PDF -4+ 2014 RDB database. The XRD gave a good qualitative measure of existing phases in the samples. This was vital to understand if the synthesis was successful, and what phases existed after pre-oxidation and reduction.

3.9.2 Electron probe micro-analysis

The reduced pellets were subjected to EPMA. Four SeriForm containers, 40 mm in diameter, with three pellets from each reduced batch were filled up with epoxy under a low-pressure atmosphere. Struers Epovac was used to create a 200-mbar atmosphere. Here the containers were filled with an epoxy, a mixture of Struers EpoFix resin and Struers EpoFix hardener, and kept for two minutes. This was done to remove any air-bubbles that might have occurred during the filling of the epoxy. The containers were kept in a ventilation cabinet over-night to let the epoxy harden. The epoxied samples were removed from their containers and cut in Struers Discotom – 2 to get a cross-section at the middle of the pellets. The surface was then grinded and polished, the program and equipment used is shown in **Table 3**, before left in a drying cabinet at 60^{O}C. The samples were inserted into a Scanning Electron Microscope (SEM) where the EPMA was conducted by operator Morten Raanes (SINTEF).

Table 3: Grinding and polishing program for EPMA-samples

Grinding				
Step #	**Paper**	**Time [s]**	**Force [N]**	**Machine**
1	Struers #1200 SiC	30	15	Struers RotoForce-4 /RotoPol-31
2	Struers #2400 SiC	30		
3	Struers #4000 SiC	180		
Polishing				
1	Struers MD Dac/Dv Dp-3µm	180	25	Struers TegraForce-5 /TegraPol-31
2	Struers MD Nap Dp-1µm	180	20	

Backscattered Electron Images (BEI) were taken at three positions, **A**, **B** and **C**, within a pellet from each reduced batch, illustrated to the left in **Figure 15**. From the BEI white and grey phases were detected. At each position, a quantitative point analysis was done on three grey and three white areas, giving the atomic ratio of the elements present. Approximately $1/4$ of each pellet was subjected to x-ray mapping of the elements, illustrated to the right in **Figure 15**. This gave the distribution of the elements.

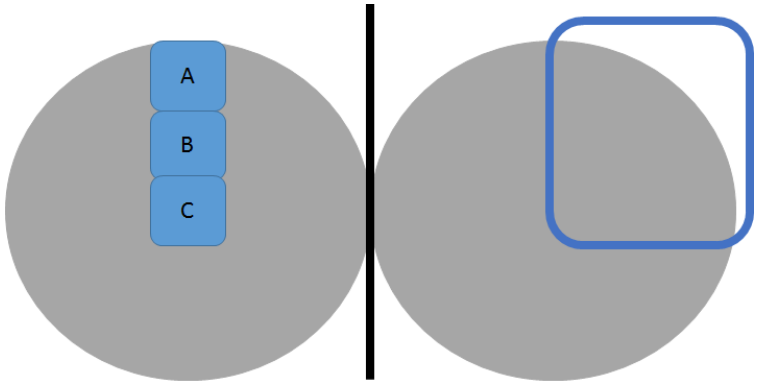

Figure 15: Sections of pellets analysed, EPMA.
BEI (left), x-ray mapping (right)

3.9.3 Particle size distribution

A powder sample from the crushed synthetic ilmenite was taken before the powder went into pelletizing. Approximately 0.2g was analysed. To remove any agglomerates the sample was first put in an ultrasound-bath. The sample was then inserted into a Coulter LS230 for analysis. The powder was dropped in water, which transports the powder through the machine. By using a laser and multiple detectors, the particle sizes were measured by laser diffraction. Large particles diffract poorly and diffraction is increased with decreasing particle size. The analysis measures particle between 0.04 – 2000µm and lasts approximately 90 seconds. This was done twice to make sure there were no discrepancies. The analyses were performed by Irene Braggstad (SINTEF).

3.10 Overview of the experiments

An overview over the successful experiments in this master's thesis is given in **Table 4** below.

Table 4: Complete overview over all experiments

Complete overview over experiments	
Briquetting	**Note**
Attempt #1.1	No heat-treatment
Attempt #1.2	Oxide-mixture
Attempt #1.3	Oxide-mixture
Attempt #2.1	Sintered
Synthesis and pre-oxidation	
Batch #1.X	Fe/Ti = 1.00, project work
Batch #3.X	Fe/Ti = 1.12, #3.3 and #3.4
Batch #4.X	Fe/Ti = 1.00, #4.1 and #4.3
Batch #5.X	Fe/Ti = 1.24, #5.3 and #5.4
Reduction	
Batch #1.X	50% CO + 50% H_2, 40 min
Batch #3.X.1	50% CO + 50% H_2, 120 min
Batch #3.X.2	100% H_2, 160 min
Batch #4.X	50% CO + 50% H_2, 160 min
Batch #5.X	50% CO + 50% H_2, 120 min

4 Results

4.1 Briquetting and sintering

Attempt #1.1: The small TiO_2 briquettes without any heat-treatment did not compress the volume sufficiently. Not all the raw material fit in the crucible.

Attempt #1.2: The small Fe_2O_3 + TiO_2 briquettes that were dried at 100°C fit in the crucible. However, heavy splashing occurred and broke the protective glass during synthesis, shown in **Figure 16**. **Attempt #1.3** had approximately the same result, but the splashing was not as violent.

Figure 16: Splashing of liquid metal on protective glass.

Attempt #2.1: The TiO_2 briquettes were sintered and had no splashing during synthesis. The smelt was well mixed for five minutes, before cooled down. This was renamed **batch #5.3**. An XRD comparing **batch #5.3** with **batch #5.4** can be seen later in this chapter, in **Figure 22**, together with further comments about **batch #5.3**.

4.2 XRD

In the XRD analysis figures, the author has used abbreviations to show the different phases. The list over these abbreviations is shown in **Table 5** below. The figures also have a colour-code, where the peaks that represent the same phases are of equal colour. However, the figures where there are comparisons between two batches this colour coding is not shown. It is important to notice that some phases are represented by more than one colour, which is due to a small difference in the lattice parameters. Keep in mind that a phase's colour change from figure to figure.

Table 5: Abbreviations for the x-ray diffraction figures

H	Hematite	Fe_2O_3
IL	Ilmenite	$FeTiO_3$
IR	Iron	Fe
PB	Pseudobrookite	Fe_2TiO_5
R	Rutile	TiO_2
RR	Reduced rutile	Ti_3O_5, Ti_4O_7, Ti_9O_{17}
US	Ulvöspinel	Fe_2TiO_4

4.2.1 Batch #4.X, Fe/Ti = 1.00

Synthesis

The synthesis of pure $FeTiO_3$ was accomplished. Results of the two successful batches can be seen in the XRD analysis in **Figure 17**. This clearly indicates that the sample consists of ilmenite according to reaction **(2)**. **Batch #4.1** and **#4.3** were mixed together, and they are hereby written **batch #4.X**.

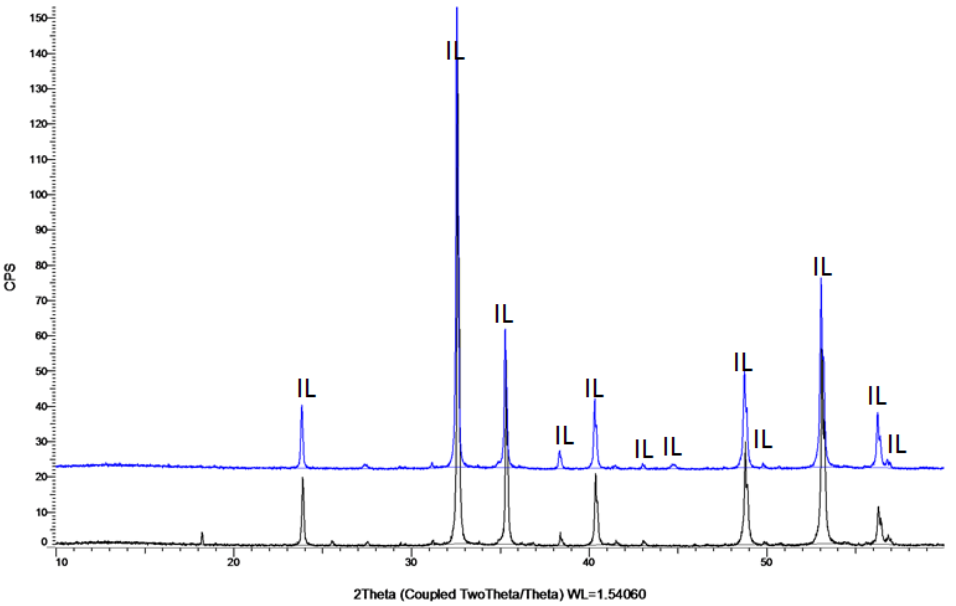

Figure 17: XRD after synthesis of batch #4.1 (bottom) and #4.3 (top).

Pre-oxidation

The XRD analysis of the pre-oxidized pellets, shown in **Figure 18**, clearly indicates the existence of TiO_2 and Fe_2TiO_5, as expected from reaction **(5)** and **(6)**. It also show some traces of Fe_2O_3. This will be discussed in Chapter 5.

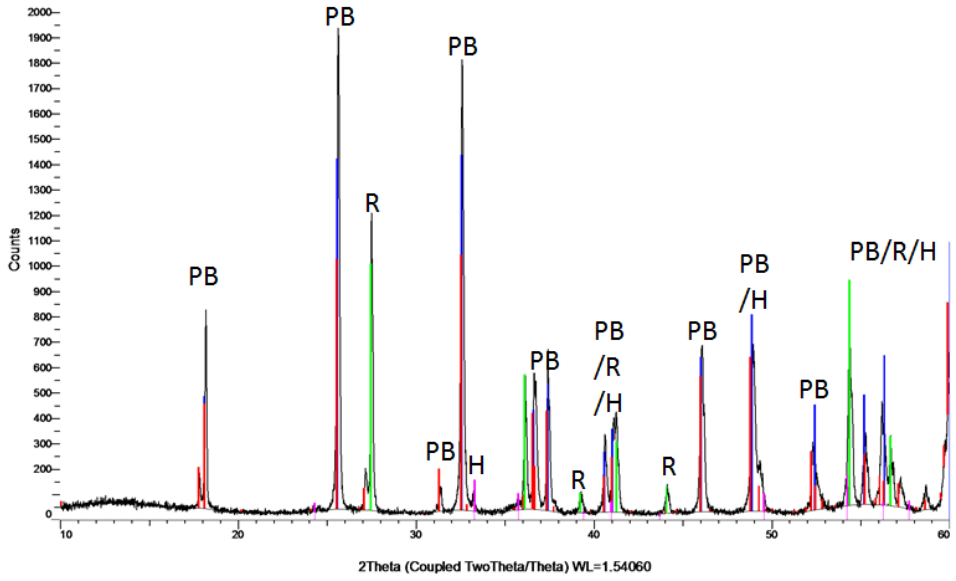

Figure 18: XRD after pre-oxidation of batch #4.X

Reduction

Figure 19 shows the phases present after reduction in a 50% CO + 50% H_2 atmosphere. It can be seen the existence of Fe and TiO_2 in the sample, which is in accordance with reaction **(7-10)**. In addition, there are traces of reduced rutile, the Magnéli phase Ti_9O_{17}, together with Fe_3C. This will be discussed in chapter 5.

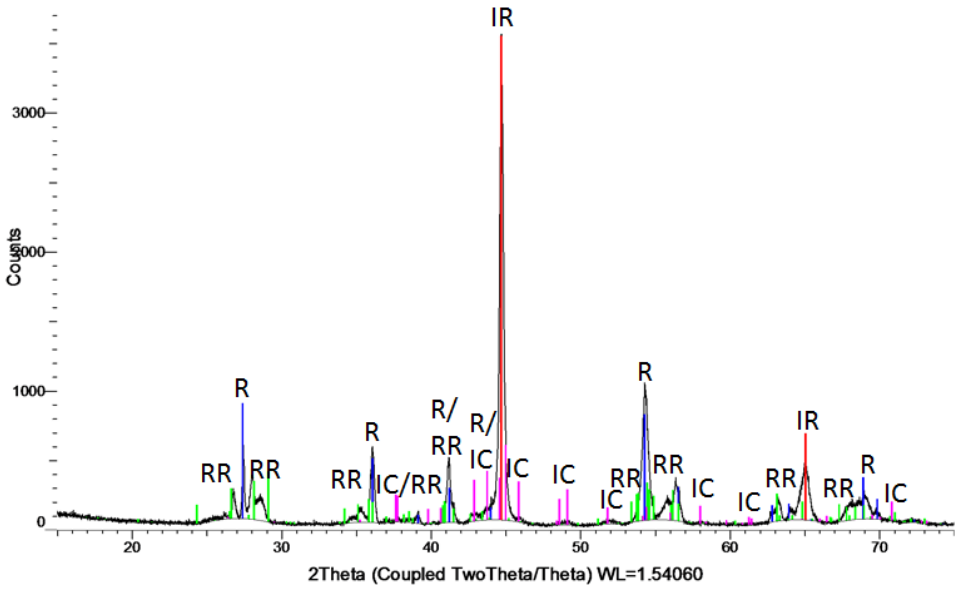

Figure 19: XRD after reduction of batch #4.X

4.2.2 Batch #3.X, Fe/Ti = 1.12

Synthesis

Figure 20 shows the XRD analysis of **batch #3.3** and **#3.4** compared. The major peaks are $FeTiO_3$, while the medium peaks are Fe_2TiO_4 and Fe. Two small peaks of TiO_2 at 27.5° and 36.5° can also be seen. Note the similarities and difference between the reference ilmenite, **Figure 17**, and **Figure 20**. The $FeTiO_3$ peaks are identical. However, in **batch #3.3** and **#3.4**, Fe_2TiO_4 and Fe are also present. **Batch #3.3** and **#3.4** were identical, mixed together and hereby written **batch #3.X**.

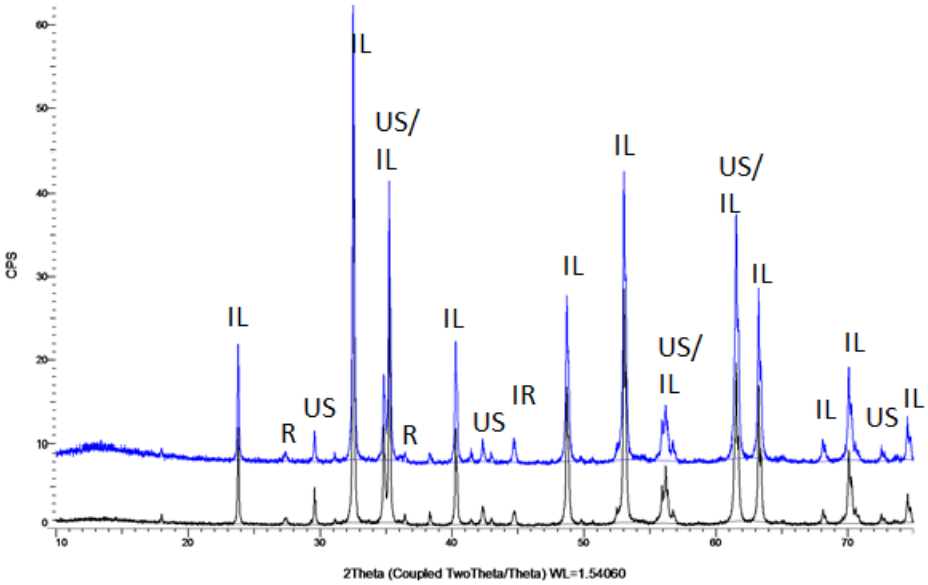

Figure 20: XRD after synthesis of batch #3.3 (bottom) and #3.4 (top).

Pre-oxidation

XRD analysis of the pre-oxidized pellets is very similar to the phases present in the pre-oxidized reference ilmenite. It shows the existence of TiO_2 and Fe_2TiO_5, together with traces of Fe_2O_3. See Appendix A.2 for XRD figure, **Figure 36**

Reduction batch #3.X.1

The reduction of **batch #3.X.1** was done under a 50% CO + 50% H_2 atmosphere. The phases present are identical to those present after reduction of the reference ilmenite, **batch #4.X**. The XRD figure can be seen in Appendix A.2, **Figure 37**.

Reduction batch #3.X.2

After reduction of **batch #3.X.2** in a pure H_2 atmosphere, Fe, TiO_2, Ti_3O_5 and Ti_4O_7 are present. This can be seen in **Figure 21**. Note the presence of reduced rutile, which is Ti_3O_5 and the Magnéli phase Ti_4O_7.

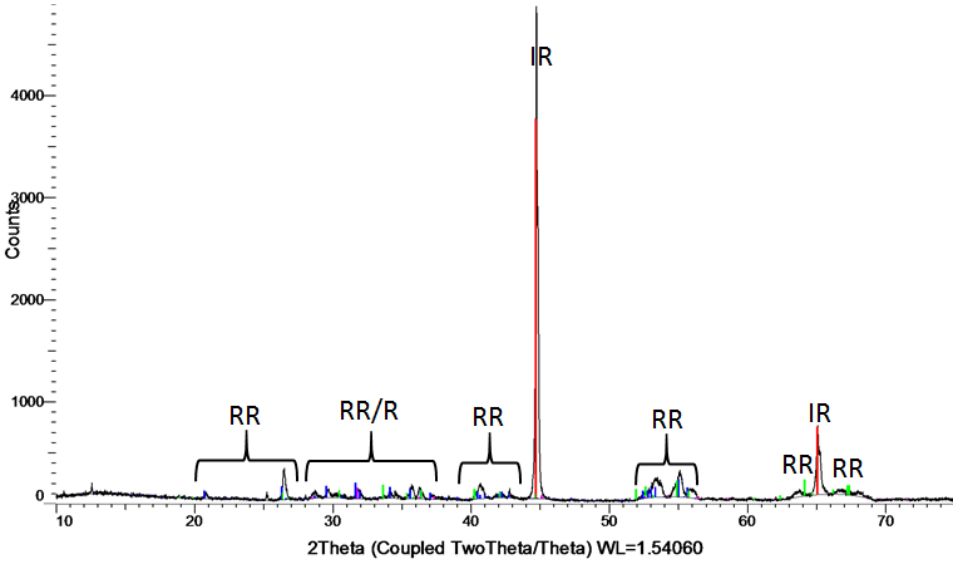

Figure 21: XRD after reduction of batch #3.X.2

The O/Ti ratios for the reduced TiO_2 – phases for **batch #3.X.1** and **#3.X.2** can be seen in **Table 6**. Note the lower O/Ti ratios for **batch #3.X.2**.

Table 6: O/Ti ratios of the reduced TiO_2 phases

Reduced TiO2			
Batch #	**O/Ti**		**Note**
3.X.1	1.889	-	Ti_9O_{17}
3.X.2	1.667	1.750	Ti_3O_5, Ti_4O_7

4.2.3 Batch #5.X, Fe/Ti = 1.24

Synthesis

Synthesis of **batch #5.3** and **#5.4** shows the presence of the same phases as for **batch #3.X**, which are $FeTiO_3$, Fe_2TiO_4 and some Fe. The XRD result is shown in **Figure 22**. Notice the similarities between **batch #5.3**, which was made from briquetted and sintered anatase, and **#5.4**. The two batches were mixed together and renamed **batch #5.X**.

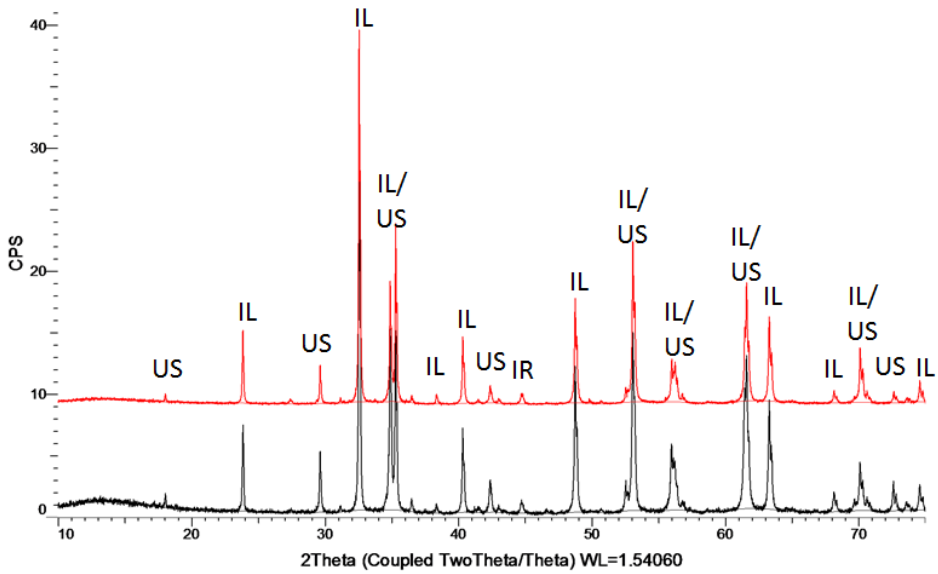

Figure 22: XRD after synthesis of batch #5.3 (top) and #5.4 (bottom).

Pre-oxidation

Similar as the pre-oxidized **batch #3.X** and **#4.X**, **batch #5.X** consists of Fe_2TiO_5, TiO_2 and Fe_2O_3. This is shown in Appendix A.2, **Figure 38**

Reduction

The reduction of **batch #5.X** was done in a 50% CO + 50% H_2 atmosphere. The XRD results show the presence of Fe, Ti_9O_{17}, TiO_2 and Fe_3C. These are the same phases as those present in **batch #3.X.1** and **#4.X**. Therefore, the XRD figure is not shown here, but can be found in Appendix A.2, **Figure 39**.

4.3 Particle size distribution

The particle size distribution of **batch #3.X**, **#4.X** and **#5.X** after crushing and before pelletizing is shown in **Figure 23**. Volume frequency is shown in **Figure 24**. The mean size is 26.57 µm for **batch #3.X**, 106 µm for **batch #4.X** and 36.98 µm for **batch #5.X**. It can be seen that **batch #5.X** and **#3.X** have approximately the same distribution, while **batch #4.X** has larger particles.

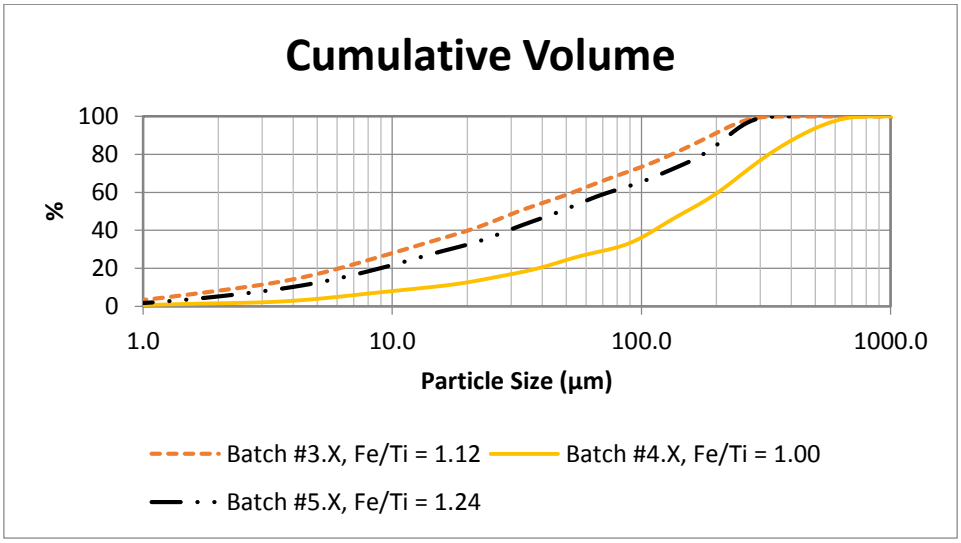

Figure 23: Particle size distribution before pelletizing, all batches

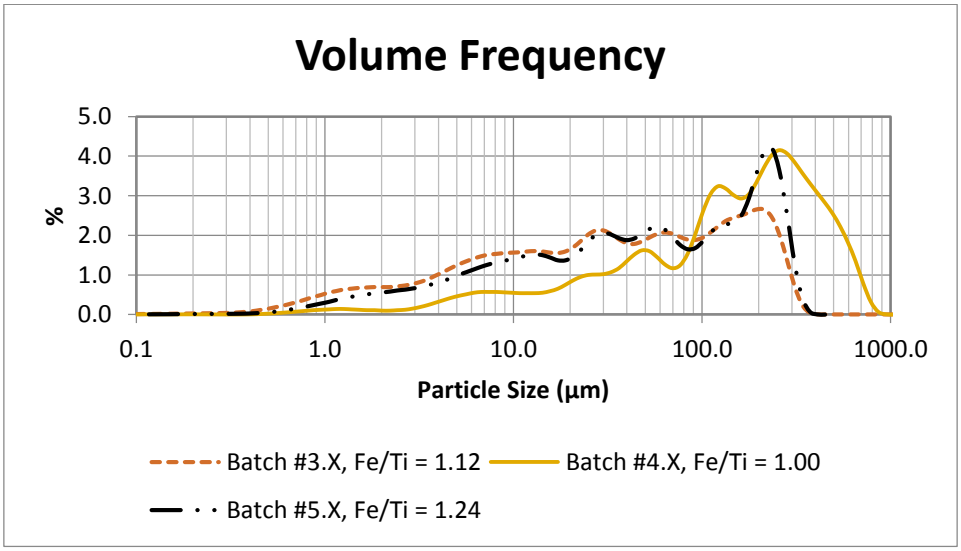

Figure 24: Volume frequency of particle sizes before pelletizing, all batches

4.4 Degree of conversion

Based on equation **(1)** and the mass-loss curves measured during reduction, the degree of conversion is calculated for all batches and shown in **Figure 25**. It can be seen that the reduction follows a steep incline the first 5 minutes, before slowing down. After approximately two hours the batches with a mixture of 50% CO + 50% H_2 gas reached its maximum and starts to slightly decline. For the pure H_2 reduction, there is a steep incline from 5 minutes until 80 minutes, before the incline is reduced. However, it is worth noticing the conversion degree is still increasing until the end of the experiment. The highest conversion degree of all experiments was achieved in **batch #3.X.2**, which is in accordance with theory. Note the trend higher Fe content indicates lower conversion degree between **batch #3.X.1** and **#4.X**, and between **#4.X** and **#5.X**, but that the trend is opposite between batch **#3.X.1** and **#5.X**. In addition, note that the degree of conversion does not exceed one in **batch #3.X.1**, **#4.X** and **#5.X**.

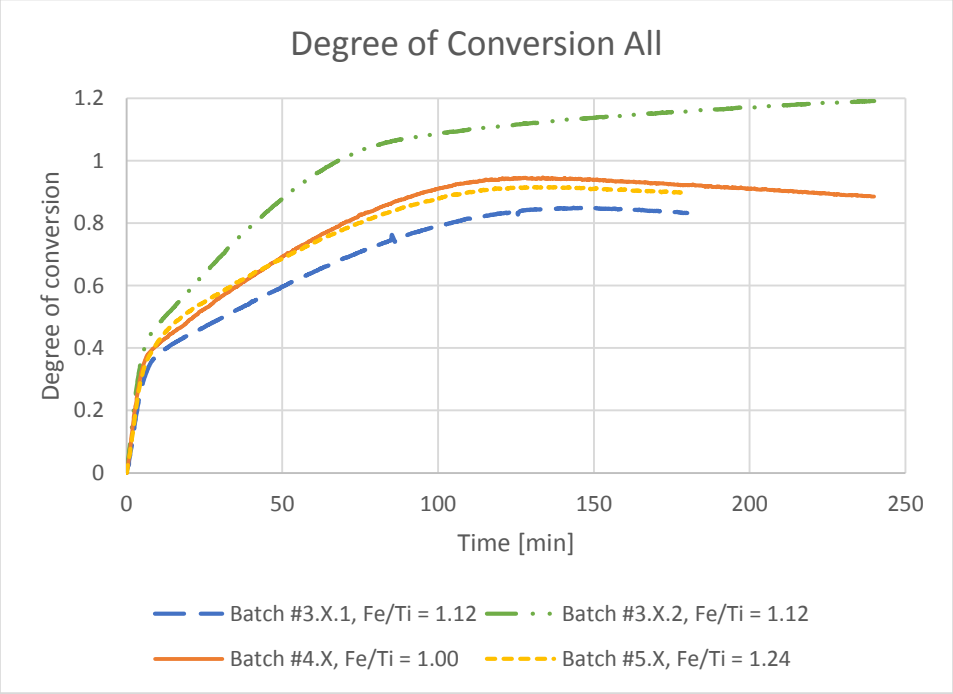

Figure 25: Degree of conversion graph for all the reduced batches.

4.5 EPMA

The SEM picture of each batch is shown in **Figure 26** below. It can be seen that all batches are porous. However, **batch #5.X** has a more porous structure than the others do. This will be discussed in the next chapter.

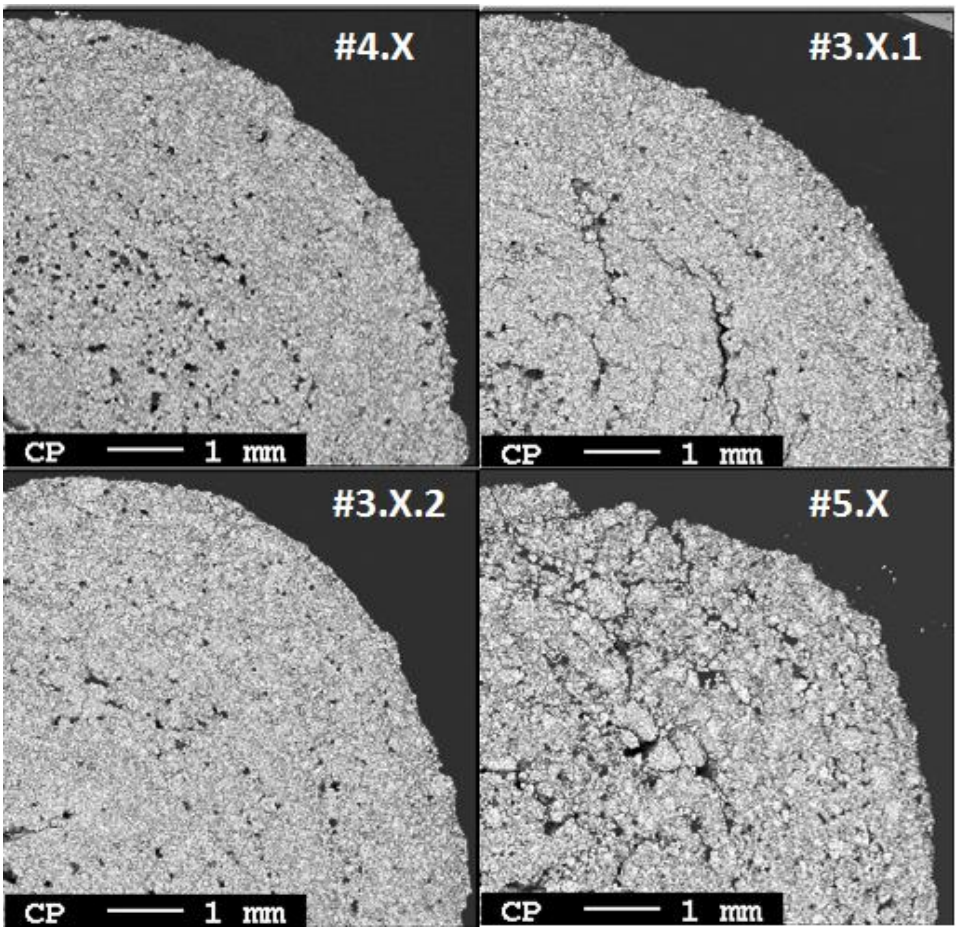

Figure 26: SEM pictures, 1/4 of a pellet.
Batch #4.X, Fe/Ti = 1.00 (top left). Batch #3.X.1, Fe/Ti = 1.12 (top right).
Batch #3.X.2, Fe/Ti = 1.12 (bottom left). Batch #5.X, Fe/Ti = 1.24 (bottom right)

X-ray mapping of a reduced pellet was similar for **batch #3.X.1**, **#3.X.2**, **#4.X** and **#5.X**. The x-ray mapping for **batch #4.X** can be seen in **Figure 27**, while the figures of the others can be found in Appendix A.3. The elements are evenly distributed throughout the pellet. Notice the existence of Si and C.

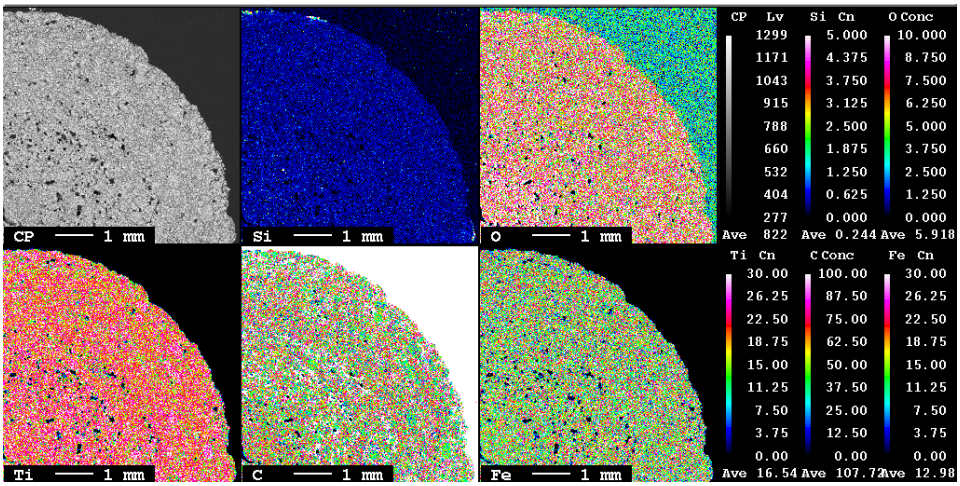

Figure 27: EPMA x-ray mapping, batch #4.X Fe/Ti = 1.00 (50% CO + 50% H_2)

X-ray mapping for the reference ilmenite is seen in **Figure 28**, **Figure 29** and **Figure 30**. **Batch #1.X** was reduced for 40 minutes, **#4.X OX** is after pre-oxidation and **#4.X RED** is after four hours reduction.

For Fe, **Figure 28**, only the outer layer is reduced after 40 minutes, while after the full four hours the whole core has reacted. The green and yellow areas in the pre-oxidized pellet, which indicates medium Fe concentration, have been changed to blue, low Fe concentration, and white, high Fe concentration.

For O, **Figure 29**, it is clear that the whole **batch #1.X** pellet have changed concentration. However, the change is more rapid near the edge, area **A**. In **batch #4.X** after full reduction, the pellet is mostly reduced, blue, with some smaller green areas.

For Ti, **Figure 30**, concentration only changes slightly. Notice the change in concentration occurring at the edge, area **A**, in **batch #1.X**.

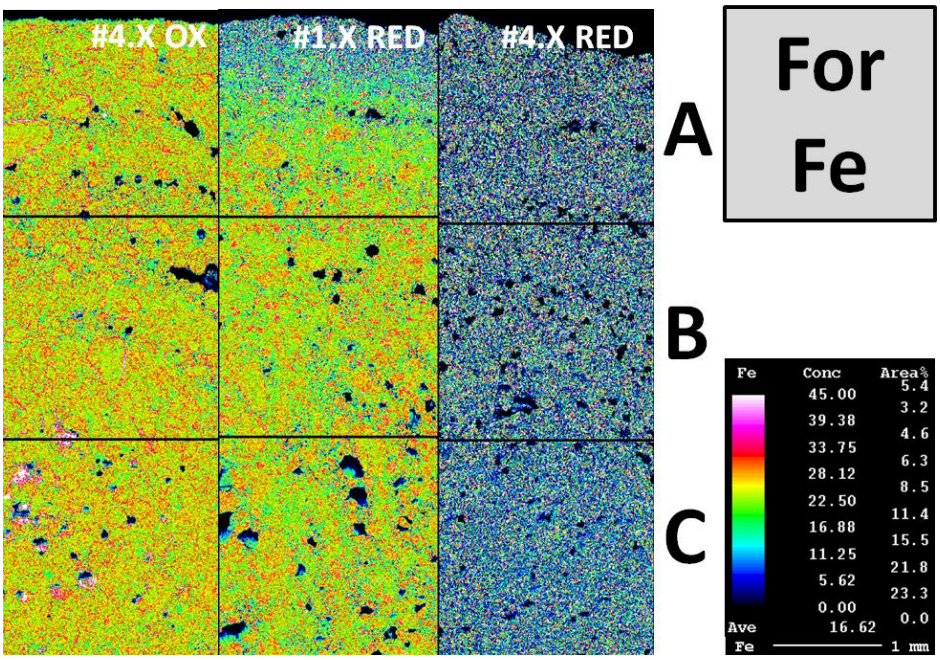

Figure 28: X-ray mapping of iron.
Batch #4.X oxidized (left), #1.X reduced (middle) and #4.X reduced (right)

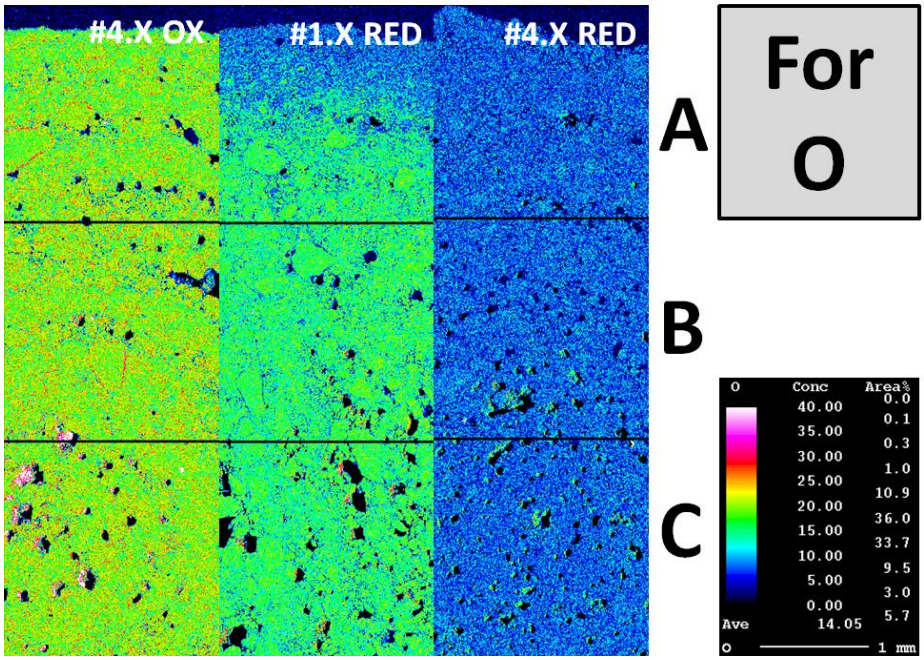

Figure 29: X-ray mapping of oxygen.
Batch #4.X oxidized (left), #1.X reduced (middle) and #4.X reduced (right)

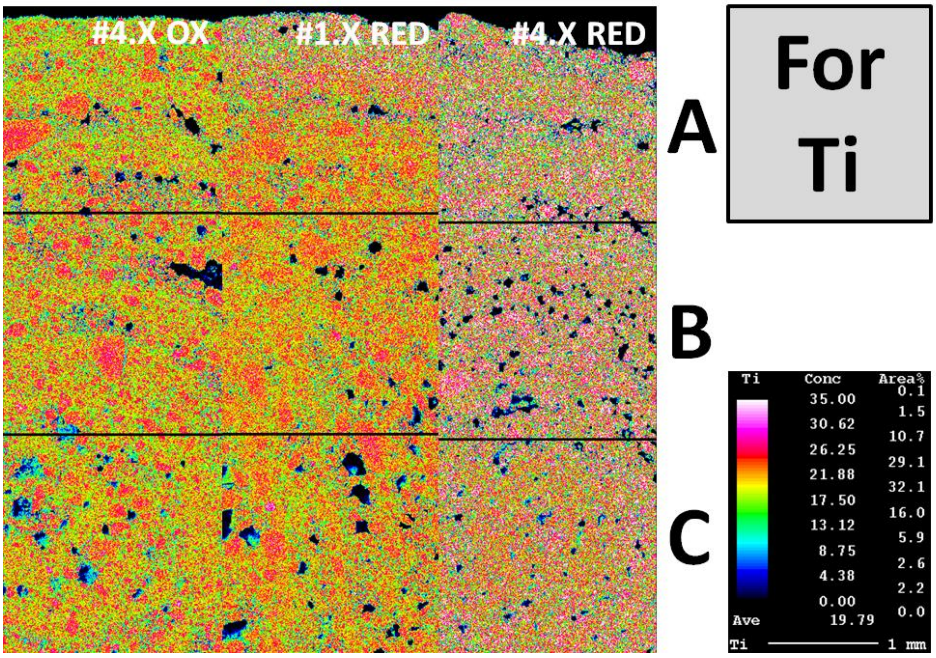

Figure 30: X-ray mapping of titanium
Batch #4.X oxidized (left), #1.X reduced (middle) and #4.X reduced (right)

BEI of **batch #4.X** and **#5.X** can be seen in **Figure 31** and **Figure 32** on the next page. Since **batch #4.X**, **#3.X.1** and **#3.X.2** were similar, only BEI of **#4.X** is shown here. The rest can be found in Appendix A.3. White is a metallic phase, while grey is an oxide phase. Black is pores and voids, which is most likely filled with epoxy. **Batch #3.X.1**, **#3.X.2** and **#4.X** all have small, encapsulated pores within the grey oxide layer, while **batch #5.X** has a lot less of these.

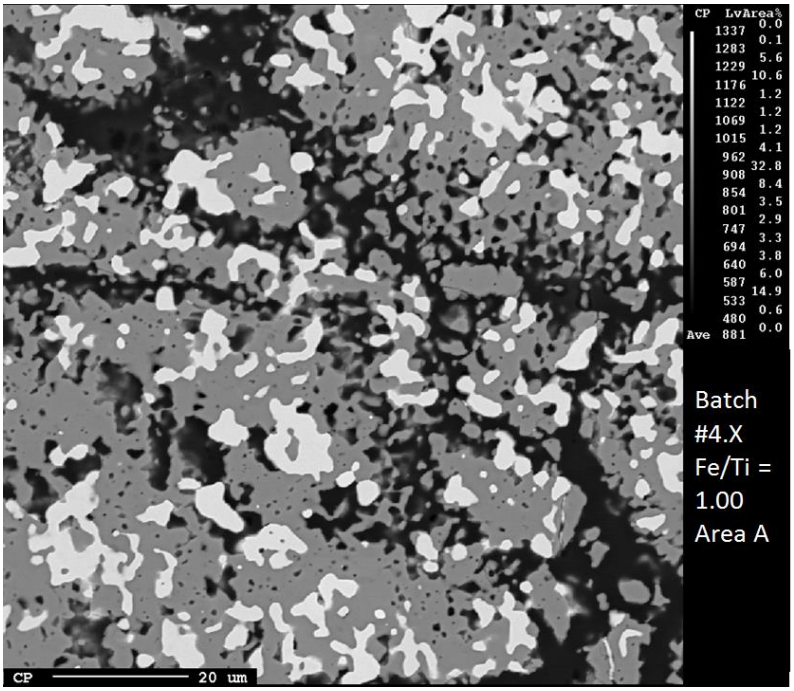

Figure 31: BEI of batch #4.X, Fe/Ti = 1.00, at area A (edge)

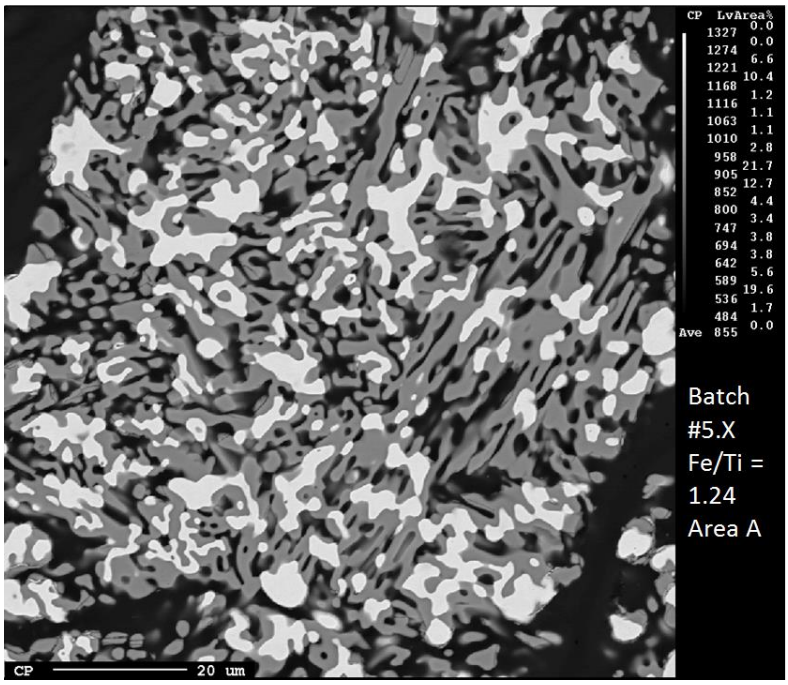

Figure 32: BEI of batch #5.X, Fe/Ti = 1.24, at area A (edge)

The quantitative point analysis gave the atomic ratio of elements present. Below in **Table 7** the average composition of Fe, Ti and O within the white and grey areas for all batches are shown. The complete atomic ratio table, **Table 14** and **Table 15**, can be found in Appendix A.3. Si was also detected, but the values were low, <1.2% atomic ratio. C was excluded due to reasons that will be mentioned in the discussion, under "*5.3.2 Carbon formation during reduction with CO*". Notice the low atomic ratio of O and Ti in the light areas, while the grey areas are low on Fe. In addition, note that the composition within the grey and white areas at position **A**, **B** and **C** were similar for all batches. Average O/Ti ratios are shown in **Table 8**. Notice that all O/Ti ratios are above two and approximately equal, with **batch #3.X.1** having a slightly higher ratio.

Table 7: Average atomic ratio for O, Ti and Fe in the light and grey areas

		Average Atomic Ratio [%]			
		Batch #4.X, Fe/Ti = 1.00	**Batch #3.X.1, Fe/Ti = 1.12 with CO + H_2**	**Batch #3.X.2, Fe/Ti = 1.12 with H_2**	**Batch #5.X, Fe/Ti = 1.24**
O	**Light area**	1.972	2.223	2.205	1.834
	Grey area	66.675	67.433	66.505	66.558
Ti	**Light area**	3.580	3.211	3.641	3.552
	Grey area	32.683	31.777	32.631	32.479
Fe	**Light area**	94.418	94.273	93.922	94.584
	Grey area	0.583	0.633	0.817	0.947

Table 8: Average O/Ti ratio in the grey areas

		O/Ti Ratio			
		Batch #4.X, Fe/Ti = 1.00	**Batch #3.X.1, Fe/Ti = 1.12 with CO + H_2**	**Batch #3.X.2, Fe/Ti = 1.12 with H_2**	**Batch #5.X, Fe/Ti = 1.24**
Grey areas	**A**	2.007	2.195	2.042	2.047
	B	2.052	2.085	2.035	2.089
	C	2.063	2.092	2.038	2.014
Average		**2.041**	**2.124**	**2.038**	**2.050**

5 Discussion

5.1 Briquetting

In **attempt #1.1** small TiO_2 briquettes without heat-treatment were used. The oxide layer was insufficiently compressed, resulting in a too full crucible. No melting was achieved with **attempt #1.1**. However, the author believes that if melting had been achieved during this attempt, splashing would have occurred. Splashing occurs because of air-voids within the oxide layer, or the formation of gases. Either the air-voids are introduced during the creation of the briquettes, or pockets of air is concealed between the particles during mixing and positioning in the crucible. In addition, residues of the stearic acid used as a lubricant during briquetting may cause problems. The C from stearic acid can react with O forming a gas, which would lead to splashing

Attempt #1.2 and **#1.3** were done with a mixture of the oxides, Fe_2O_3 + TiO_2, briquetted and dried at 100°C. By the amount of splashing observed during synthesis, seen in **Figure 16**, it is clear that voids, defects and residual stearic acid introduced during briquetting were not removed during the low temperature heat-treatment. According to theory, extra voids would also be introduced due to the similarity of the particle sizes, enhancing the splashing. This is supported by the success of **attempt #2.1**.

In **attempt #2.1,** TiO_2 was briquetted and sintered at 900°C, which lowered the volume of the total oxide sufficiently to fit in the crucible. The size difference between the oxides was high enough to reduce voids created during mixing. In addition, sintering at 900°C over 15 hours proved sufficient in terms of removing residual stearic acid and most of the voids within the briquettes.

In short, **attempt #1.1** - **#1.3** were unsuccessful, while **#2.1** was a success. Based on these results, it is clear the importance of briquetting and sintering.

5.2 Synthesis and pre-oxidation

Synthetic ilmenite and Fe rich ilmenite was successfully synthesised as the XRD analyses shows. The aim was to have the excess Fe as Fe_2TiO_4, which was achieved. A small amount of Fe can be seen, which indicates a slight invasion of the three-phased area "2" in **Figure 4**. However, the amount is considered too low to create problems during the succeeding steps. As seen from **Figure 18,** pre-oxidation fully oxidized the Fe. This figure is representative for all batches in terms of phases present after pre-oxidation. The major components are Fe_2TiO_5 and TiO_2, which is consistent with the phase diagram, shown in **Figure 5**. From the existence of Fe_2O_3, it appears that during oxidation the two-phase area Fe_2O_3 – Fe_2TiO_5 was slightly invaded. However, all the Fe was in their Fe^{3+} state, which means Fe_2O_3 does not have any negative effect on the next step, reduction.

5.3 Reduction

The quantitative point analysis, shown in **Table 7**, indicates that the white metallic phase is mostly Fe. Since the amount of the other elements are so low compared to Fe, it is unlikely that Fe is tied to any oxygen. This is supported by the XRD analysis, shown in **Figure 19** and **Figure 21**. In addition, the quantitative point analysis indicates the grey areas to be consisting of titanium oxides with an approximate O/Ti-ratio of two. From the EPMA and XRD analysis, it is therefore clear that all batches were fully reduced. However, the average O/Ti ratio is above two, approximately equal for all batches and does not indicate the presence of reduced TiO_2. An explanation can be that the pellets and areas analysed in the EPMA are not completely representative for the whole batch. **Batch #3.X.2**, reduced with 100% H_2, has according to XRD analysis more reduced TiO_2 than the others and should have a lower O/Ti-ratio. However, according to **Table 8**, the O/Ti ratio for **batch #4.X**, **#3.X.2** and **#5.X** are approximately equal. In addition, **batch #3.X.1** has an unexpected higher O/Ti-ratio. These results cannot be explained by the author at the current time. A larger quantity of pellets are required to be analysed to get a clearer understanding of this.

According to **Figure 28**, **Figure 29** and **Figure 30** it is clear from the change in concentration throughout the pellet that reduction was complete for **batch #4.X**. This is supported by the XRD analysis, **Figure 19**. The x-ray mapping of the elements indicates that the rate of reduction occurs more rapidly near the edges, area **A**. This can be seen in all three x-ray mapping figures. In **batch #1.X**, the concentration change is higher at area **A** then at area **B** and **C**. This is in accordance with the shrinking core model. In **Figure 28** and **Figure 29,** it is clear that Fe and O is being reduced at area **B** and **C** even after 40 minutes. The reducing gas penetrates and reduces the particles within area **B** and **C**, although at a slower rate than for area **A**. This indicates that the shrinking core model should not only be applied on a macro scale, the whole pellet, but also on a micro scale, locally on all particles throughout the pellet. Porosity will enhance the accessibility of reducing gas towards the centre. In addition, it will increase the rate of reduction as long as enough reducing gas is available. Porosity is further discussed later in this chapter, under "*5.4 Particle size distribution*".

Even though **Figure 27** shows the existence of Si, the amount of Si detected is very low, with the highest values detected being approximately one atomic percent near the edge. Si is believed to be an impurity introduced during the sample preparation for the EPMA. A possible source is residue from the grinding, where SiC-paper was used. Si has therefore been ignored in this discussion.

5.3.1 The impact of H_2 for iron rich ilmenite

According to **Figure 33** below, which is based on **Figure 25**, it is clear that the reduction of ilmenite by H_2 and CO + H_2 can be divided into three phases. The first incline is steep and over a short period, and is similar for both **batch #3.X.1** and **#3.X.2**. Here Fe^{3+} is reduced to Fe^{2+}, which is a quick reduction. Therefore, the different reducing gases do not significantly affect the reduction rate at this stage.

The second, longer, incline is the metallization Fe^{2+} to Fe. It can be seen that for **batch #3.X.2** all Fe^{2+} is converted into metallic Fe approximately 50 minutes ahead of **#3.X.1**. During the third phase of reduction, **batch #3.X.1** increases weight slightly. This, together with why the degree of conversion does not reach one during phase two for reduction where CO is used, is discussed later in "*5.3.2 Carbon formation during reduction with CO*".

According to the XRD analysis, small amounts of TiO_2 is reduced to Ti_9O_{17} for **batch #3.X.1**. For **batch #3.X.2**, there is still mass loss during the third phase of reduction. The mass loss occurs at a slower rate than during phase two, indicating that TiO_2 is harder to reduce. This is in accordance with literature. **Table 6** clearly shows that a lower O/Ti ratio is reached for **batch #3.X.2** compared to **#3.X.1**, supporting the results from **Figure 33** below.

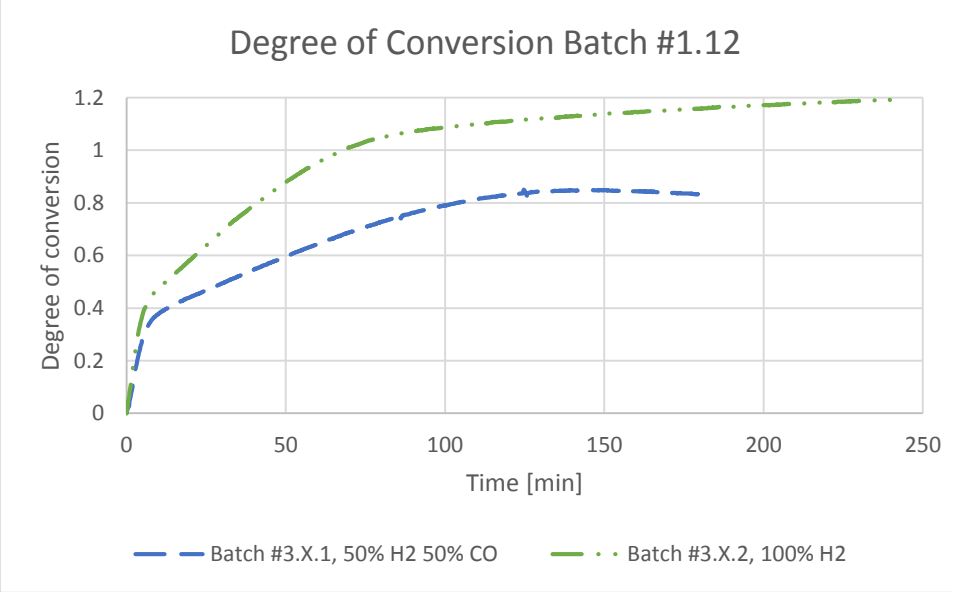

Figure 33: Degree of conversion for batch #3.X.1 and #3.X.2.

It is clear from the results of this master's thesis that H_2 is a better reducing gas than CO for the reduction rate of ilmenite. H_2 penetrates and reduces the pellets at a faster rate than CO during phase two. In addition, 100% H_2 continues to reduce TiO_2 to a more reduced TiO_2 than 50% CO + 50% H_2 during phase three. After four hours, the degree of conversion graph for 100% H_2 shows no indication to reduce its rate of reduction. However, this is believed to stagnate after it reaches a certain O/Ti-ratio. The ratio and time required to reach this ratio was not studied in this work. A reduction over a longer period has to be conducted.

5.3.2 Carbon formation during reduction with CO

For the reduction experiments where 50% CO + 50% H_2 was used, **batch #3.X.1**, **#4.X** and **#5.X**, reduction is completed after approximately two hours. At longer reduction time, a small weight-increase can be seen. One explanation can be the formation of soot, or C. According to the Boudouard-reaction, **(11)**, when there is no more Fe – oxide to reduce, the activity shifts to the right side of the equation. In addition, Fe works as a catalyst for the Boudouard reaction. This leads to C being deposited on the sample and retort wall. Since **batch #3.X.2** is reduced without any CO, only H_2, it also explains why the degree of conversion curve for this batch does not have a weight gain during the third phase of reduction.

From **Figure 25** it can be seen that the degree of conversion does not reach one for those batches where 50% CO + 50% H_2 was used, **batch #3.X.1**, **#4.X** and **#5.X**. Soot formation can explain why the weight loss is not high enough. The author calculated the required weight gained from CO during reduction to account for the low degree of conversion, and the numbers are presented in **Table 9** below. According to this, a substantial amount of C has to be deposited on the sample and retort wall. The soot left in the retort measured after reduction for **batch #5.X** was approximately 0.35g, while the soot formed during reduction of the other batches was not measured, but is believed to be of approximately the same weight. The amount of C deposited have to be four to thirteen times higher to account for the lack of weight loss. Therefore, soot alone is not the explanation.

Table 9: Extra mass loss required for a degree of conversion = 1.00

Mass loss [g] required to reach Degree of Conversion = 1.00		
Batch #4.X, Fe/Ti = 1.00	**Batch #3.X.1, Fe/Ti = 1.12**	**Batch #5.X, Fe/Ti = 1.24**
1.61	4.76	2.79

One explanation can be seen from the XRD analysis in **Figure 19**. This gives indication of some Fe reacting with C, forming Fe_3C. This is also in accordance with literature [16]. Since Fe works as a catalyst for the Boudouard reaction, by increasing the Fe in the sample, more C is deposited and will subsequently react with the Fe. This will reduce the mass loss measured during the experiments. **Table 10** shows the calculations to reach a degree of conversion of unity by the formation of Fe_3C, assuming 0.35g of soot in the retort after reduction and that $13.9625\ g\ Fe/g\ C$ is required for the formation of Fe_3C.

Table 10: Calculations of Fe tied to C after reduction

	To reach degree of conversion = 1.00 [g]		
	Batch #4.X, Fe/Ti = 1.00	**Batch #3.X.1, Fe/Ti = 1.12**	**Batch #5.X, Fe/Ti = 1.24**
Possible C tied to Fe	1.26	4.41	2.44
Total Fe in red. sample	70.26	74.03	77.38
Fe tied to C, required	17.57	61.51	34.10
Pure Fe left in sample	**52.69**	**12.52**	**43.28**

According to the XRD analyses after reduction, there seems to be very little Fe_3C. By comparing the calculations in **Table 10** with the XRD peaks for Fe_3C, it is clear that the formation of Fe_3C does not solely explain the low degree of conversion. For example, **batch #3.X.1** clearly has more than 12.52g of pure Fe left in the sample after reduction according to the XRD analyses. It is a more plausible explanation for **batch #4.X**, however, further analysis of the reduced pellets is required to test this. In addition, the theory above cannot be used to explain why **batch #5.X** has a higher mass loss than **#3.X.1**, since the extra Fe should result in more C being deposited, leading to a lower mass loss.

EPMA has problems detecting carbides. Therefore, based on this analysis the existence of Fe_3C phase cannot be determined. The major amount of C detected in the EPMA is from the epoxy, which fills up the pores within the material giving too high values of C. Due to this C detected in the EPMA was ignored. Other analyses have to be done to determine with safety the existence of a Fe_3C-phase or other carbide phases. However, according to theory [16], Fe – carbides can be created during reduction.

Another explanation for the low degree of conversion can be explained by extra Fe loss after each step that precede reduction. An assumption in this work is whenever material has been lost during the synthesis, crushing, pelletizing and pre-oxidation; it has been equal moles of Fe and Ti. If there is a loss of extra Fe compared to Ti during these steps, this can be used to explain the low degree of conversion for **batch #3.X.1**, **#4.X** and **#5.X**. However, a substantial amount of extra Fe has to be lost, approximately 4-6g depending on the batch. This is considered highly unlikely by the author. An analysis of material lost after each step have to be evaluated to confirm or disprove this theory.

The author believes a mixture of the theories above best explains why **batch #3.X.1**, **#4.X** and **#5.X** do not reach degree of conversion equal to one in **Figure 25**. However, these theories requires further testing.

5.3.3 The impact of excess iron

The removal of **batch #3.X.2** from **Figure 25** results in **Figure 34** below. This shows how the Fe content influence the reduction rate. It can be seen that Fe/Ti = 1.12 has a lower rate of reduction and degree of conversion than Fe/Ti = 1.00. The author believed Fe/Ti = 1.24 would follow the same trend, but this is clearly not the case. Fe/Ti = 1.24 has a reduction rate approximately equal that of the reference ilmenite.

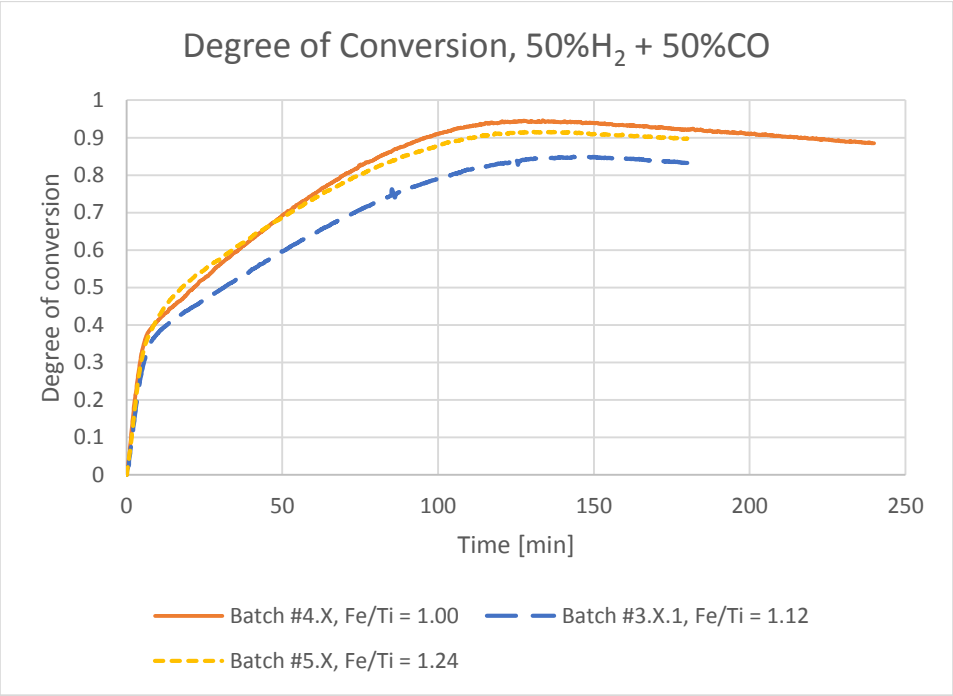

Figure 34: Degree of conversion for batches reduced with 50% CO + 50% H_2

One theory is that Fe inhibits the rate of reduction up to a certain Fe/Ti-ratio, where a further increase of the Fe/Ti-ratio enhances the reduction rate. This theory is based on work done by Zhao and Shadman [17, 18], which states that two mechanisms control the reduction rate. The first mechanism is that metallic Fe will form a shell around the particles and fill up pores within the TiO_2 – layer, which will hinder the reducing gas to interact with the unreduced oxide. This results in the reduction rate being hindered with increasing amount of Fe in the sample. Here, diffusion through the ash layer is rate-limiting, which is the second and forth step in the shrinking core model.

A second mechanism enhances the reduction rate, which is diffusion of metallic Fe towards other metallic Fe. This opens up the pores and pathways within the pellets, enabling the reducing gas to react with the unreduced oxide. With a higher Fe concentration, the rate of diffusion increases, enhancing the reduction. The second and forth step in the shrinking core model will no longer be rate-limiting. An indication for this mechanism can be the lack of small encapsulated pores within the grey oxide layers for **batch #5.X**, Fe/Ti = 1.24, while all the other batches do have these pores. This can be seen in **Figure 31** and **Figure 32**. In addition, the above theory is supported by the more porous structure in **batch #5.X**, seen in **Figure 26.**

According to **Figure 34**, it is clear that the first mechanism is dominant up to Fe/Ti = 1.12, while the second mechanism overtakes the dominance somewhere between Fe/Ti = 1.12 and 1.24. However, exactly at what ratio these mechanism switches dominance was not determined. To find this ratio, experiments where all other parameters are kept constant with different Fe/Ti-ratios between 1.12 and 1.24 have to be done. A sketch of how the author believes the relationship between inhibiting the rate of reduction and excess Fe is can be seen in **Figure 35** below. The first inhibiting mechanism is dominant during the first incline, until reaching a Fe/Ti-ratio between 1.12 and 1.24. Here, the second mechanism becomes dominant, which enhances the rate of reduction. At a certain point of excess Fe, further increasing the Fe/Ti-ratio will again inhibit the rate of reduction due to shell formation around the particles.

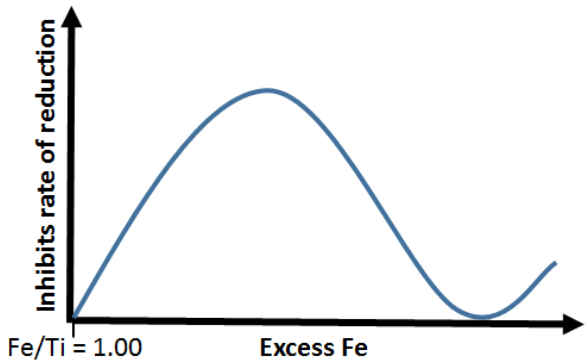

Figure 35: Author's sketch of how excess Fe inhibits the rate of reduction

As a side note, there is no evidence that any Fe/Ti >1.00 will get a higher degree of conversion than for Fe/Ti = 1.00. The author finds this to be highly unlikely.

5.4 Particle size distribution

Particle size distribution is believed to influence the rate of reduction. Porous structures are reduced more easily than non-porous structures, due to easier access to the unreduced areas for the reducing gas. With equal sized particles, the structure will have larger voids, which increases the porosity. However, particle size distribution will also influence the pelletizing. Little diversity in the particle sizes introduces problems with creating spherical pellets during pelletizing. The optimal particle size distribution to enhance the reduction of ilmenite is currently unknown for the author. However, there is literature suggesting optimal mixture of a material consisting of two different particle sizes. A ratio of 2/3 coarse particles and 1/3 fine particles, where the larger size difference the better, is optimal [19]. This can serve as a starting point for future studies. However, according to theory, pre-oxidation enhances porosity and will have little effect on already porous pellets. It is therefore unsure to what extent the particle size distribution influences the rate of reduction.

During this work **batch #3.X**, Fe/Ti = 1.12, and **#5.X**, Fe/Ti = 1.24, had quite similar distributions. **Batch #4.X**, Fe/Ti = 1.00, had larger particles, resulting in a larger particle size distribution interval. This can be seen in **Figure 23** and **Figure 24.** The reason behind this difference is not completely understood by the author, since crushing time was kept constant. The difference indicates extra Fe enhances the crushing and helps with crushing the largest particles. Since **batch #3.X** and **#5.X** had similar distribution, it cannot be used to explain the unexpected difference in the degree of conversion graph discussed earlier this chapter, and why **batch #5.X** appeared to have a more porous structure after reduction.

To identify the impact of the particle size distribution has on reduction, all other parameters have to be kept equal. Ilmenite has to be synthesised with a constant Fe/Ti-ratio, only changing the crushing time. In addition, results from this master's thesis indicates that extra Fe influence the crushing, which must be further studied. Batches with slightly different Fe/Ti-ratios must be made and the crushing time kept constant to understand this mechanism.

6 Conclusion

Fe rich ilmenite was successfully made by adding equal moles of Fe_2O_3 and metallic Fe. To get a successful smelt from two oxide powders, one of the oxides have to be briquetted and sintered in order to optimize the packing and to remove any voids created during briquetting. Sintering TiO_2 at 900°C over 15 hours proved to be sufficient to get a successful ilmenite smelt in the CCIF.

Excess Fe inhibits the rate of reduction for ilmenite. This study shows that excess Fe inhibits the reduction rate of ilmenite up to a certain Fe/Ti-ratio, whereby increasing the Fe content another mechanism that enhances the rate of reduction becomes dominant. However, this theory requires further work. In addition, there is no evidence that any amount of extra Fe will get a higher degree of conversion than that for Fe/Ti = 1.00.

The degree of conversion did not exceed one in any batches where CO were present, indicating unreduced Fe. However, analysis showed no presence of Fe – oxide. By using CO in the reducing gas the formation of soot occurs, which increases the weight slightly and impacts the degree of conversion calculated. In addition, the C deposited on the sample during reduction appears to react with metallic Fe and create Fe_3C in the sample, which reduces the measured mass loss.

XRD results shows the presence of reduced TiO_2 in all batches. However, pure H_2 produces a more reduced TiO_2, Ti_3O_5 and Ti_4O_7, than 50% H_2 + 50% CO, Ti_9O_{17}. This is supported by the degree of conversion graphs, showing a considerable higher rate of reduction and conversion degree for reduction with pure H_2. Therefore, it is clear that by adding H_2 to the reducing gas, reduction rate and conversion degree is enhanced substantially.

The particle size distribution affects the porosity, which will subsequently affect the rate of reduction. Higher porosity enhances the reduction rate. However, further studies are needed to understand at what degree the particle size distribution affects the reduction rate.

7 Future work

The author suggests the following to be looked into:

- To see the effect the crushing time, the different particle size distributions and Fe have on the rate of reduction. This can be done by:
  - Keep the Fe/Ti-ratio constant, but change the crushing time. This will give an indication on how the particle size distribution is changed by the crushing time.
  - Use the powder from above and create equal sized pellets. Keep pre-oxidation conditions, reduction sample size and reducing gas composition constant.
  - Slightly change the Fe/Ti-ratio and keep the crushing time constant. See if excess Fe influences the particle size distribution.
- Explanations for why the degree of conversion does not exceed one for 50% CO + 50% H_2 should be looked into. The formation of Fe_3C is one possible explanation and requires further work.
- More experiments with high Fe/Ti-ratios to confirm or disprove the theory where excess Fe goes from inhibiting to enhancing the rate of reduction.
- In addition, the impact of lower than one Fe/Ti-ratio is of great interest due to the utilization of sand ilmenite mines. Synthesis of batches with low Fe content is believed to be possible in the experimental setup used during this master's thesis.

Together these results will create a more in-depth picture of the mechanisms controlling how different Fe/Ti-ratios influence the solid-state reduction behaviour of ilmenite.

References

1. Norhaug, S., *Impurities in Ilmenite, Excess Iron*. 2014, NTNU: Project work at Departement of Materials Science and Engineering.
2. Rankin, W.J., *Minerals, Metals and Sustainability: Meeting future material needs*. 2011, CSIRO publishing. p. 70-71.
3. U.S. Geological Survey. 2014 [cited 2014 30th of November]; Available from: http://minerals.usgs.gov/minerals/pubs/commodity/titanium/mcs-2014-timin.pdf.
4. Grande Côte Operation. 2015 [cited 2015 25th of May]; Available from: http://www.tizir.co.uk/projects-operations/grande-cote-mineral-sands/.
5. Sahu, K.K., et al., *An overview on the production of pigment grade titania from titania-rich slag.* Waste management & research, 2006. **24**(1): p. 74-79.
6. Noubactep, C., *Metallic iron for environmental remediation: Learning from the Becher process.* Journal of Hazardous Materials, 2009. **168**(2–3): p. 1609-1612.
7. Folmo, G. and D. Rierson. *Ilmenite direct reduction project in Norway using the Grate-Car process*. in *Ironmaking Conference Proceedings*. 1992.
8. Lobo, S.C., L. Kolbeinsen, and S. Seim, *Reduction of Ilmenite with Synthesis Gas*, in *Heavy Minerals Conference*. 2013.
9. Sun, K., R. Takahashi, and J.-I. Yagi, *Reduction kinetics of cement-bonded natural ilmenite pellets with hydrogen.* ISIJ international, 1992. **32**(4): p. 496-504.
10. Canaguier, V.Y., *Synthesis of ilmenite*. 2014, NTNU: Master thesis at Department of Materials Science and Engineering.
11. Michud, C., *Processing, properties, and performance in use of direct reduced ilmenite pellets*. 2007, NTNU: Department of Materials Science and Engineering.
12. Jones, D.G., *Kinetics of gaseous reduction of ilmenite.* Journal of Applied Chemistry and Biotechnology, 1975. **25**(8): p. 561-582.
13. Fu, X., Y. Wang, and F. Wei, *Phase transitions and reaction mechanism of ilmenite oxidation.* Metallurgical and Materials Transactions A, 2010. **41**(5): p. 1338-1348.
14. Jones, D., *Reaction sequences in the reduction of ilmenite: 2-gaseous reduction by carbon monoxide.* Trans. Inst. Min. Metall.(Section C), 1973. **82**: p. C186-C192.

15. Wei, X., et al., *Phase transitions, micro-morphology and its oxidation mechanism in oxidation of ilmenite (FeTiO 3) powder.* Transactions of Nonferrous Metals Society of China, 2013. **23**(8): p. 2439-2445.
16. Kucukkaragoz, C.S. and R.H. Eric, *Solid state reduction of a natural ilmenite.* Minerals Engineering, 2006. **19**(3): p. 334-337.
17. Zhao, Y. and F. Shadman, *Kinetics and mechanism of ilmenite reduction with carbon monoxide.* AIChE Journal, 1990. **36**(9): p. 1433-1438.
18. Zhao, Y. and F. Shadman, *Reduction of ilmenite with hydrogen.* Industrial & engineering chemistry research, 1991. **30**(9): p. 2080-2087.
19. von Bogdandy, L. and H.J. Engell, *Die Reduktion der Eisenerze: wissenschaftliche Grundlagen und technische Durchführung*. 1967: Springer-Verlag.
20. Richerson, D., D.W. Richerson, and W.E. Lee, *Modern ceramic engineering: properties, processing, and use in design*. 2005, CRC press. p. 477-526.
21. Fang, Z.Z., *Sintering of advanced materials*. 2010, Elsevier. p. 4-9.
22. Hahn, H., J. Logas, and R.S. Averback, *Sintering characteristics of nanocrystalline TiO2.* Journal of Materials Research, 1990. **5**(03): p. 609-614.
23. Borowiec, K. and T. Rosenqvist, *Phase relations and oxidation studies in the system Fe-Fe2O3-TiO2 at 700-1100°C*. 1981, [S.l.]: [s.n.]. p. 217-224
24. Itoh, S., *Phase equilibria in the titanium-iron-oxygen system in the temperature range of 1 173 to 1 373 K.* ISIJ international, 1999. **39**(11): p. 1107-1115.
25. Pistorius, P., *Fundamentals of freeze lining behaviour in ilmenite smelting.* Journal of the South African Institute of Mining and Metallurgy, 2003. **103**(8): p. 509-514.
26. Seim, S., *Experimental Investigations and Phase Relations in the Liquid FeTiO3-Ti2O3-TiO2 Slag System*. 2011, NTNU: PhD thesis.
27. Levenspiel, O., *The chemical reactor omnibook*. 1989, Distributed by OSU Book Stores: Corvallis, OR. p. 51.1-55.25.
28. Levenspiel, O., *Chemical reaction engineering*. 1999, Wiley: New York. p. 566-588.
29. Yagi, S. and D. Kunii, *Fluidized-solids reactors with continuous solids feed—III: Conversion in experimental fluidized-solids reactors.* Chemical Engineering Science, 1961. **16**(3): p. 380-391.
30. Forsmo, S.P.E., *Oxidation of magnetite concentrate powders during storage and drying.* International Journal of Mineral Processing, 2005. **75**(1–2): p. 135-144.
31. Ramachandra Rao, C., *The anatase-rutile transition. Part 1.—Kinetics of the transformation of pure anatase.* Transactions of the Faraday Society, 1958. **54**: p. 1069-1073.

32. Gennari, F. and D. Pasquevich, *Kinetics of the anatase–rutile transformation in TiO2 in the presence of Fe2O3.* Journal of Materials Science, 1998. **33**(6): p. 1571-1578.
33. Stearic acid. 2015 [cited 2015 12th of May]; Available from: http://www.sigmaaldrich.com/catalog/product/sial/175366?lang=en&region=NO.
34. Zhao, D., *Processing and properties of direct reduced iron pellets containing material for control of steel structure*. 2010, NTNU: PhD thesis.

Appendix A – Tables, XRD and EPMA

A.1 Reduction experiments

Table 11: Experimental conditions during reduction of batch #3.X.2

Total time [HH:MM:SS]	Time interval [HH:MM:SS]	Furn. temp. [^{O}C]	H_2 [l/min]	Ar [l/min]	Furn. pos. [up/down]
00:00:10	00:00:10	22	0	1.0	Down
01:45:10	01:45:00	958	0	1.0	Up
01:55:10	00:10:00	958	0	5.0	Up
05:55:10	04:00:00	958	5.0	0.0	Up
05:55:20	00:00:10	22	0	1.0	Down
06:55:20	01:00:00	22	0	1.0	Down

Table 12: Experimental conditions during reduction of batch #3.X.1 and #5.X

Total time [HH:MM:SS]	Time interval [HH:MM:SS]	Furn. temp. [^{O}C]	CO [l/min]	H_2 [l/min]	Ar [l/min]	Furn. pos. [up/down]
00:00:10	00:00:10	22	0	0	1.0	Down
01:45:10	01:45:00	958	0	0	1.0	Up
01:55:10	00:10:00	958	0	0	5.0	Up
04:55:10	03:00:00	958	2.5	2.5	0	Up
04:55:20	00:00:10	22	0	0	1.0	Down
05:55:20	01:00:00	22	0	0	1.0	Down

Table 13: Experimental conditions during reduction of batch #4.X

Total time [HH:MM:SS]	Time interval [HH:MM:SS]	Furn. temp. [^{O}C]	CO [l/min]	H_2 [l/min]	Ar [l/min]	Furn. pos. [up/down]
00:00:10	00:00:10	22	0	0	1.0	Down
01:45:10	01:45:00	958	0	0	1.0	Up
01:55:10	00:10:00	958	0	0	5.0	Up
05:55:10	04:00:00	958	2.5	2.5	0	Up
05:55:20	00:00:10	22	0	0	1.0	Down
06:55:20	01:00:00	22	0	0	1.0	Down

A.2 Extra XRD figures and tables

Batch #3.X, Fe/Ti = 1.12

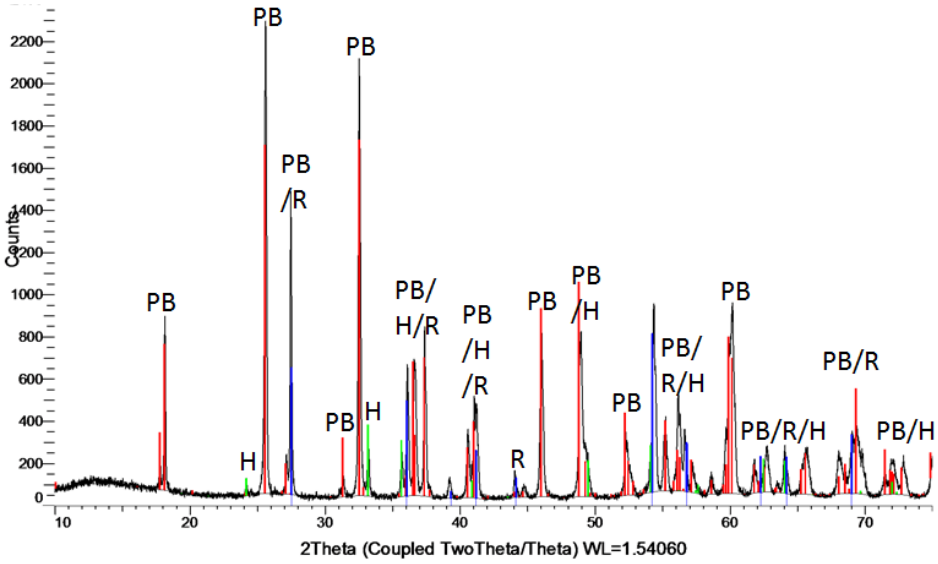

Figure 36: XRD after pre-oxidation of batch #3.X.

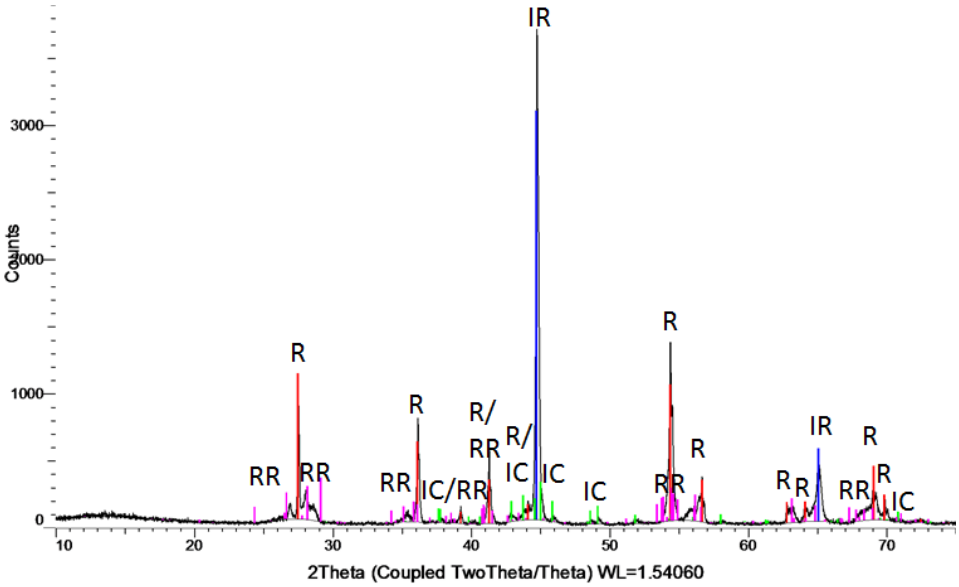

Figure 37: XRD after reduction of batch #3.X.1.

Batch #5.X, Fe/Ti = 1.24

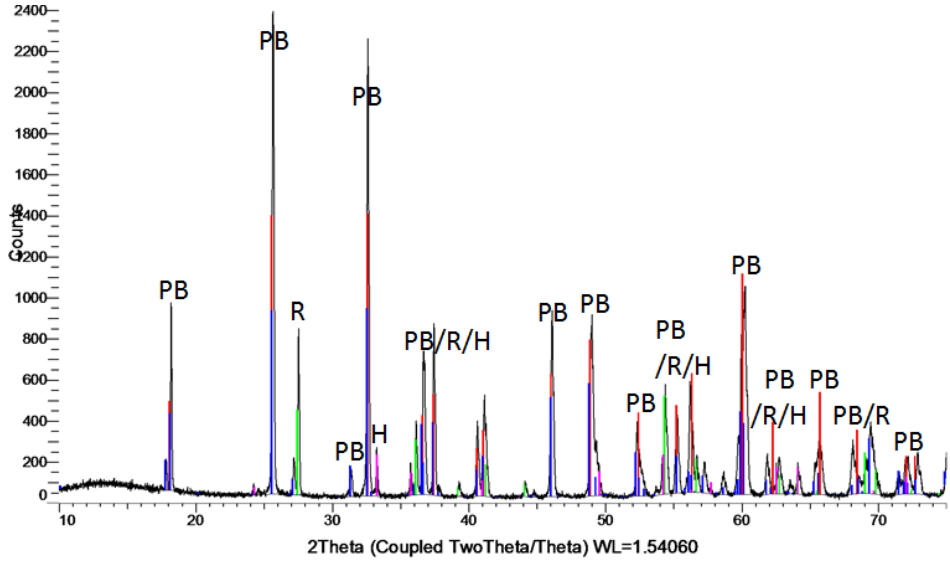

Figure 38: XRD after pre-oxidation of batch #5.X

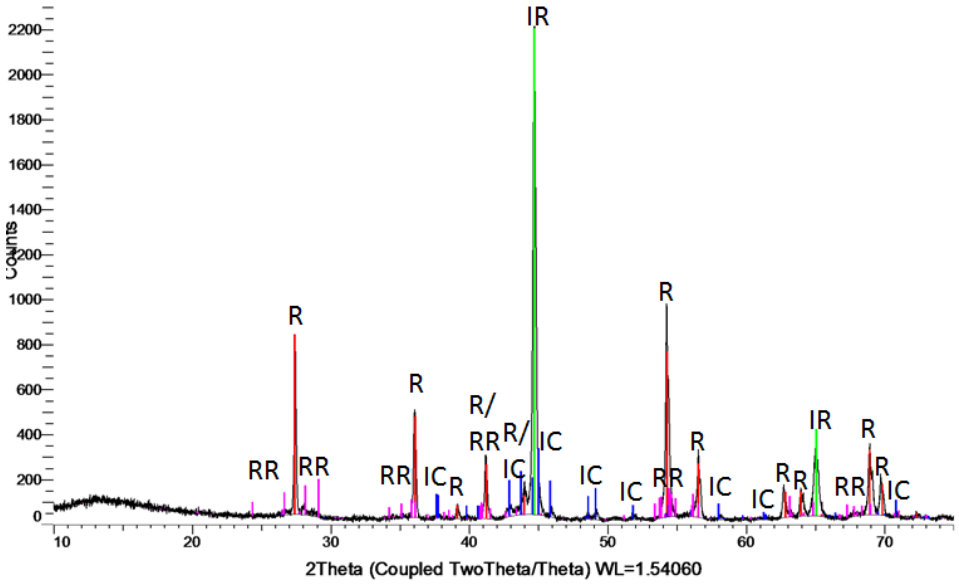

Figure 39: XRD after reduction of batch #5.X

A.3 Extra EPMA figures

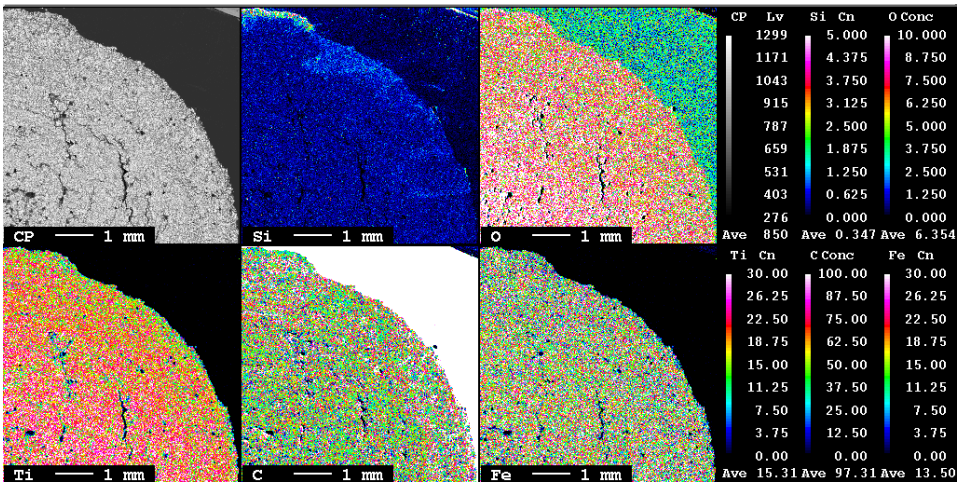

Figure 40: EPMA x-ray mapping, batch #3.X.1 Fe/Ti = 1.12 (50% H_2 + 50% CO)

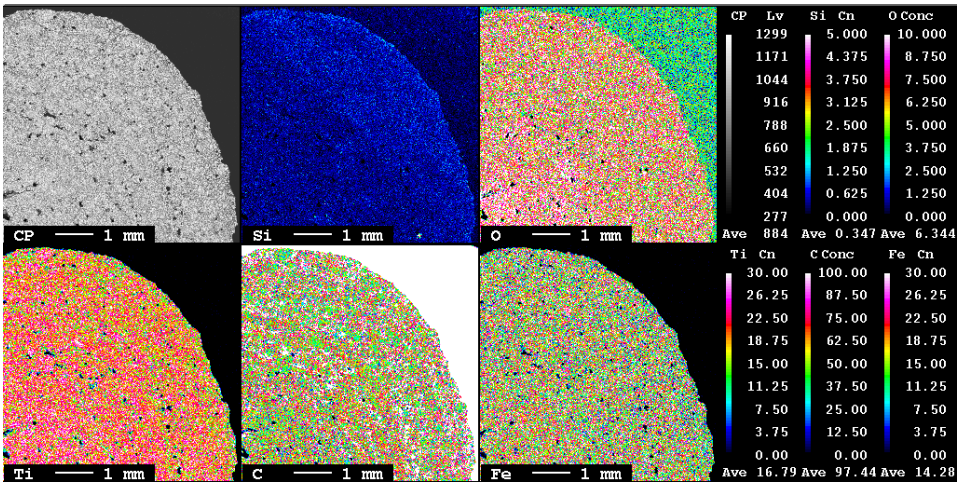

Figure 41: EPMA x-ray mapping, batch #3.X.2 Fe/Ti = 1.12 (100% H_2)

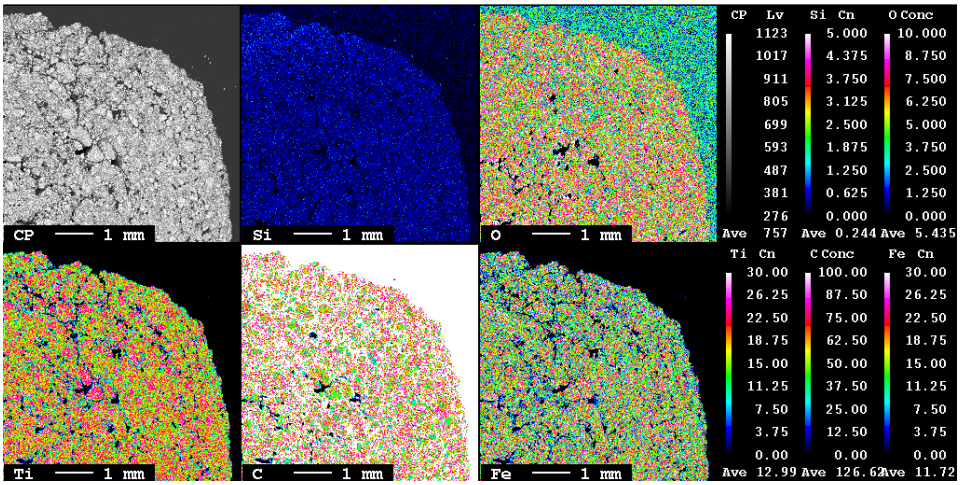

Figure 42: EPMA x-ray mapping, batch #5.X Fe/Ti = 1.24

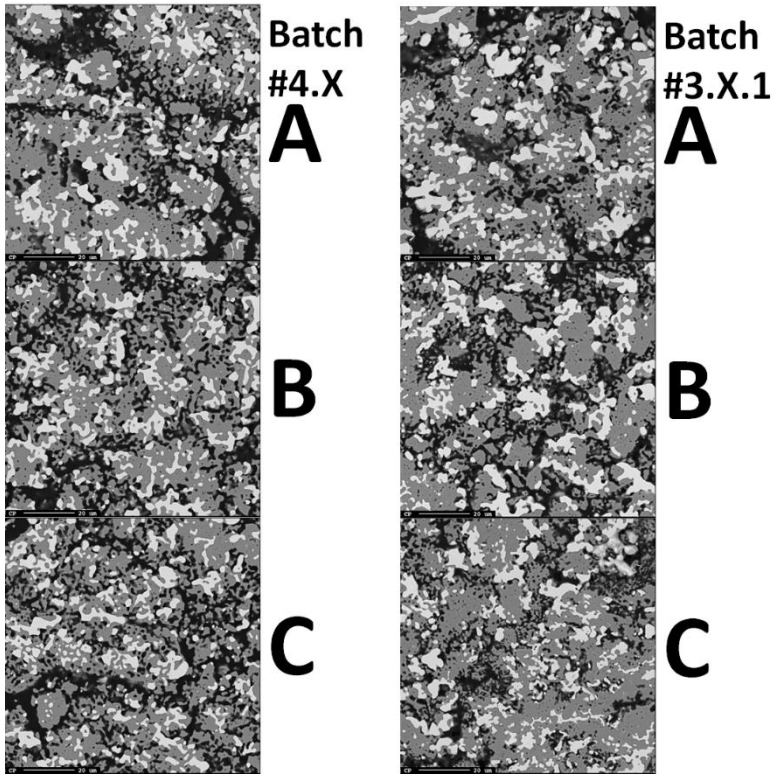

Figure 43: BEI at A, B and C.
Batch #4.X, Fe/Ti = 1.00 (left). Batch #3.X.1, Fe/Ti = 1.12 (right)

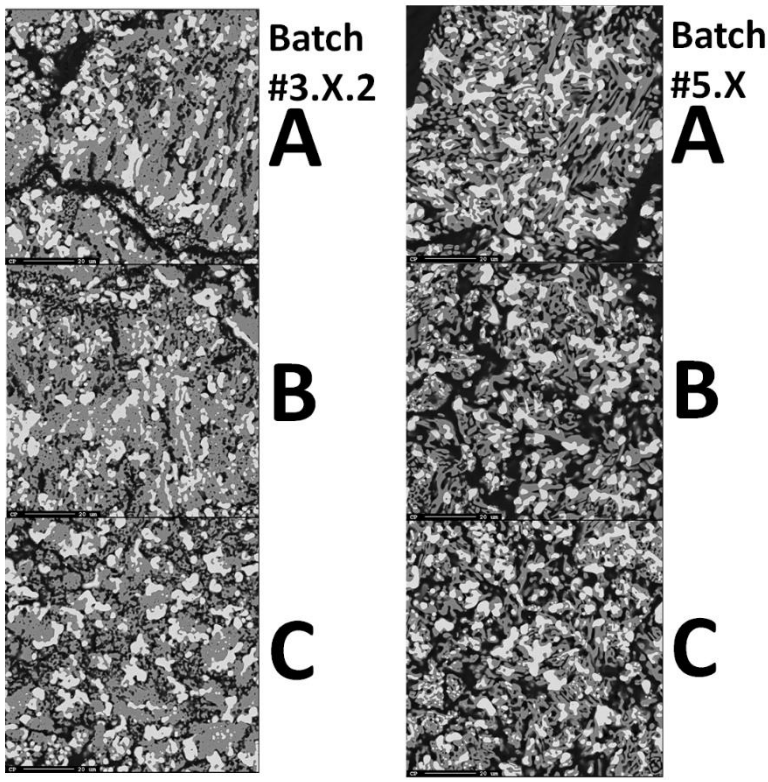

Figure 44: BEI at A, B and C.
Batch #3.X.2, Fe/Ti = 1.12 (left). Batch #5.X, Fe/Ti = 1.24 (right)

Table 14: Quantitative point analysis, batch #3.X.2 and #3.X.1

No.	Si	O	Ti	Fe	Total	Comment
1	0.2975	2.7121	3.5873	93.4032	100.00	1.12H2.A.1
2	0.4518	3.0435	3.7244	92.7804	100.00	1.12H2.A.2
3	1.0116	4.3504	3.3672	91.2708	100.00	1.12H2.A.3
4	0.1152	66.7453	32.404	0.7355	100.00	1.12H2.A.4
5	0.1377	66.3821	32.8678	0.6124	100.00	1.12H2.A.5
6	0.0924	66.6638	32.5761	0.6676	100.00	1.12H2.A.6
7	0.1095	1.8395	4.0894	93.9617	100.00	1.12H2.B.1
8	0.0524	1.3366	3.7444	94.8666	100.00	1.12H2.B.2
9	0.1676	1.7375	3.6609	94.434	100.00	1.12H2.B.3
10	0.0306	66.4193	32.8909	0.6592	100.00	1.12H2.B.4
11	0	66.1106	32.1625	1.7269	100.00	1.12H2.B.5
12	0.0433	66.3194	32.6912	0.9461	100.00	1.12H2.B.6
13	0	1.8555	3.5357	94.6088	100.00	1.12H2.C.1
14	0	1.3423	3.473	95.1848	100.00	1.12H2.C.2
15	0	1.624	3.5893	94.7867	100.00	1.12H2.C.3
16	0	66.8692	32.5144	0.6164	100.00	1.12H2.C.4
17	0	66.5901	32.6872	0.7228	100.00	1.12H2.C.5
18	0.0084	66.4425	32.8815	0.6676	100.00	1.12H2.C.6
19	0.8444	3.0043	3.0569	93.0943	100.00	1.12CO/H2.A.1
20	0.6262	2.6682	3.4254	93.2802	100.00	1.12CO/H2.A.2
21	1.1195	2.9947	2.784	93.1018	100.00	1.12CO/H2.A.3
22	0.3537	67.1301	31.7993	0.7169	100.00	1.12CO/H2.A.4
23	0.5948	67.2253	31.2282	0.9517	100.00	1.12CO/H2.A.5
24	0.3938	69.2614	29.8356	0.5093	100.00	1.12CO/H2.A.6
25	0	1.9461	3.223	94.8309	100.00	1.12CO/H2.B.1
26	0	1.9995	3.4418	94.5587	100.00	1.12CO/H2.B.2
27	0.0313	1.7807	3.8248	94.3633	100.00	1.12CO/H2.B.3
28	0.0149	67.0242	32.3797	0.5812	100.00	1.12CO/H2.B.4
29	0.0047	67.4297	32.0617	0.5038	100.00	1.12CO/H2.B.5
30	0	67.1764	32.2742	0.5494	100.00	1.12CO/H2.B.6
31	0.013	2.3217	2.6363	95.029	100.00	1.12CO/H2.C.1
32	0	1.6378	3.1844	95.1777	100.00	1.12CO/H2.C.2
33	0	1.6575	3.3222	95.0203	100.00	1.12CO/H2.C.3
34	0.0306	67.034	32.1933	0.7421	100.00	1.12CO/H2.C.4
35	0	67.4744	32.0218	0.5038	100.00	1.12CO/H2.C.5
36	0.0192	67.1444	32.198	0.6384	100.00	1.12CO/H2.C.6

Table 15: Quantitative point analysis, batch #4.X and #5.X

No.	Si	O	Ti	Fe	Total	Comment
37	0.0105	2.5543	6.1351	91.3001	100.00	1.00.A.1
38	0	1.1006	3.0737	95.8257	100.00	1.00.A.2
39	0.2606	2.4861	3.4284	93.825	100.00	1.00.A.3
40	0.0544	66.1892	33.2592	0.4973	100.00	1.00.A.4
41	0.0406	66.9725	32.2244	0.7626	100.00	1.00.A.5
42	0.1385	65.6924	33.6502	0.5188	100.00	1.00.A.6
43	0	1.1912	3.5869	95.222	100.00	1.00.B.1
44	0	2.5434	3.3372	94.1194	100.00	1.00.B.2
45	0	1.6883	2.8982	95.4135	100.00	1.00.B.3
46	0.0169	66.7989	32.5886	0.5956	100.00	1.00.B.4
47	0	66.7679	32.734	0.4981	100.00	1.00.B.5
48	0.0053	66.9683	32.3979	0.6285	100.00	1.00.B.6
49	0	2.7467	3.5611	93.6922	100.00	1.00.C.1
50	0	1.5605	3.0923	95.3473	100.00	1.00.C.2
51	0	1.8808	3.1053	95.0139	100.00	1.00.C.3
52	0.0133	67.0636	32.3713	0.5518	100.00	1.00.C.4
53	0.0142	66.5562	32.8432	0.5864	100.00	1.00.C.5
54	0.2538	67.0661	32.0755	0.6047	100.00	1.00.C.6
55	0.0716	2.179	3.1519	94.5975	100.00	1.24.A.1
56	0	1.2551	3.2077	95.5372	100.00	1.24.A.2
57	0.0429	1.6645	3.3472	94.9454	100.00	1.24.A.3
58	0.0638	64.6055	31.6227	3.708	100.00	1.24.A.4
59	0.059	66.4757	32.875	0.5903	100.00	1.24.A.5
60	0	67.0876	32.3341	0.5783	100.00	1.24.A.6
61	0	1.3714	3.1524	95.4762	100.00	1.24.B.1
62	0.0347	1.1769	3.2716	95.5169	100.00	1.24.B.2
63	0	1.5806	3.6176	94.8018	100.00	1.24.B.3
64	0.0035	66.5861	32.8503	0.5601	100.00	1.24.B.4
65	0	67.8492	31.57	0.5808	100.00	1.24.B.5
66	0.0214	67.1122	32.1012	0.7653	100.00	1.24.B.6
67	0.0505	3.137	5.042	91.7705	100.00	1.24.C.1
68	0	1.8281	3.6726	94.4994	100.00	1.24.C.2
69	0.0629	2.3168	3.5067	94.1136	100.00	1.24.C.3
70	0	66.4733	32.9407	0.586	100.00	1.24.C.4
71	0.0035	66.3553	33.1073	0.5339	100.00	1.24.C.5
72	0	66.4757	32.9076	0.6167	100.00	1.24.C.6

Appendix B – Shrinking Core Model

B.1 Gas flow through the gas film as the rate-limiting step

Whenever the resistance through the gas film is higher than the other resistances, equation **(15)** represents the rate-limiting step and the concentration profile will follow **Figure 45**. The driving force is the concentration difference between the gas film and the ash layer, $C_{A,g} - C_{A,s}$. During reaction $C_{A,s} = 0$, which leads to $C_{A,g} - C_{A,s} = C_{A,g}$.

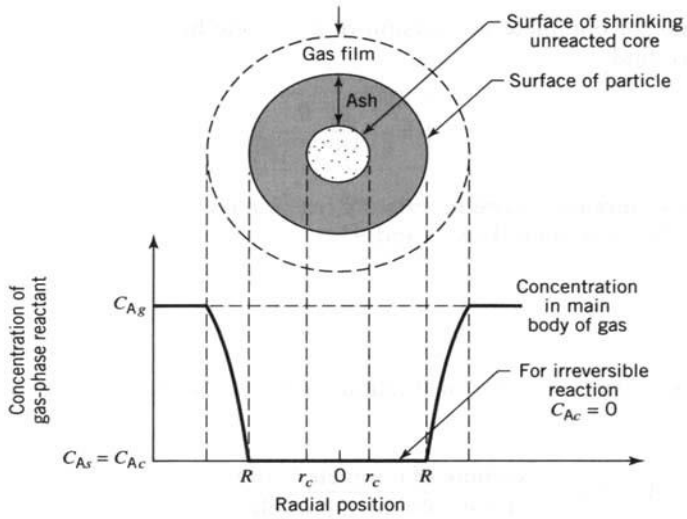

Figure 45: Gas flow through the gas film

By using the following relationships:

$$dN_B = bdN_A, \qquad N_B = \rho_B V, \qquad V = \frac{4}{3}\pi {r_c}^3, and\ S_{exterior} = 4\pi R^2 \tag{18}$$

You get:

$$-\frac{\rho_B {r_c}^2}{R^2}\frac{dr_c}{dt} = bk_g C_{A,g} \tag{19}$$

By rearranging and integrating, we find the following:

$$\frac{t}{\tau} = X_B, where\ \tau = \frac{R\rho_B}{3bk_g C_{A,g}}\ and\ X_B = 1 - \left(\frac{r_c}{R}\right)^3 \tag{20}$$

B.2 Diffusion of gas through the product layer as the rate-limiting step

When equation **(16)** is the rate-limiting step, the concentration profile will follow **Figure 46**. To get an expression of $\frac{t}{\tau}$ as above one must first consider the flux relationship for a typical partially reacted particle and then integrate r_c between 0 to R. When considering a shrinking core for particles of unchanging size in a gas/solid system, the flow rate is about 1000 times higher than the shrinkage of the core. It is therefore safe to assume that the core is stationary, which means the rate of reaction is given by the rate of diffusion to the unreacted core surface.

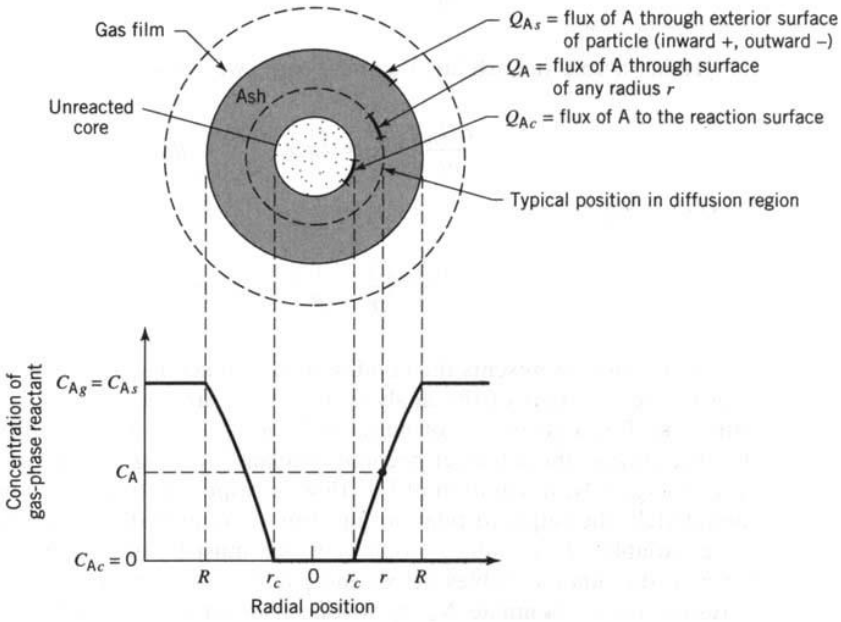

Figure 46: Diffusion of gas through the product layer

With this in mind one can derive an expression for $\frac{t}{\tau}$:

$$-\frac{dN_A}{dt} = 4\pi r^2 Q_A = 4\pi R^2 Q_{A,s} = 4\pi {r_c}^2 Q_{A,c} \qquad \textbf{(21)}$$
$$= constant, with\ Q_A = D_e \frac{dC_A}{dr}$$

By combining and integrating across the ash layer, we get:

$$-\frac{dN_A}{dt}\left(\frac{1}{r_c}-\frac{1}{R}\right)=4\pi D_e C_{A,g} \quad \textbf{(22)}$$

The second thing to consider is the shrinking of the core with time. When the core shrinks, the ash layer gets thicker, which means the diffusion of 'A' decreases. By integrating **(22)** with time, and using the relationship:

$$N_A=\rho_A V, where\ V=\frac{4}{3}\pi r^3 \quad \textbf{(23)}$$

We get:

$$\begin{aligned}\frac{t}{\tau}= & \ 1-3\left(\frac{r_c}{R}\right)^2+2\left(\frac{r_c}{R}\right)^3 \quad \textbf{(24)}\\ & =1-3(1-X_B)^{\frac{2}{3}}+2(1-X_B), where\ \tau\\ & =\frac{\rho_B R^2}{6bD_e C_{A,g}}\end{aligned}$$

B.3 Chemical reaction on the interface between the product layer and the unreacted core as the rate-limiting step

The concentration profile when equation **(17)** is the rate-limiting step is shown in **Figure 47**. The rate of reaction is unaffected by the ash layer, and is therefore proportional to the unreacted core surface.

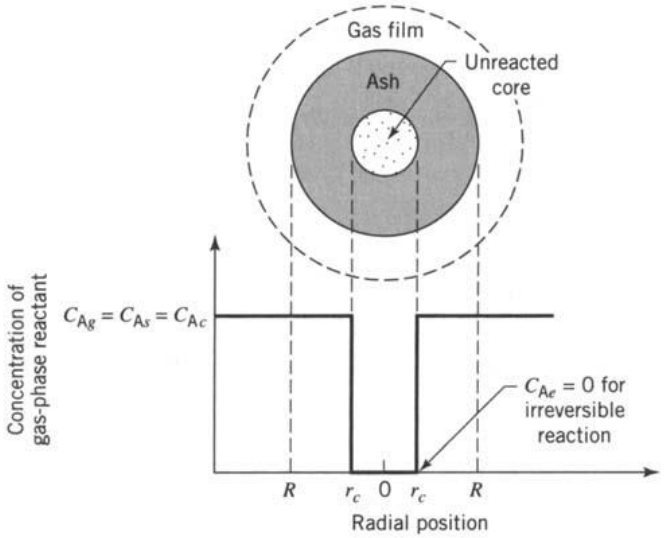

Figure 47: Chemical reaction on the interface between the product layer and the unreacted core

To get an expression for $\frac{t}{\tau}$, one start with the following equation:

$$-\frac{1}{4\pi {r_c}^2}\frac{dN_A}{dt} = -\frac{b}{4\pi {r_c}^2}\frac{dN_A}{dt} = bk_s C_{A,g} \quad \textbf{(25)}$$

By using:

$$N_A = \rho_A V, where\ V = \frac{4}{3}\pi r^3 \quad \textbf{(26)}$$

The following can be derived:

$$-\rho_B \frac{dr_c}{dt} = bk_s C_{A,g} \quad \textbf{(27)}$$

Which leads to, after integration:

$$\frac{t}{\tau} = 1 - \frac{r_c}{R} = 1 - (1 - X_B)^{1/3}, where\ \tau = \frac{\rho_B R}{bk_s C_{A,g}} \quad \textbf{(28)}$$